Title
Complex Microparticle Fabrication Using Optical Transient Liquid Molding and Cell Microcarriers

Author
Wu, Chueh-Yu

Publication Date
2016

Peer reviewed|Thesis/dissertation

UNIVERSITY OF CALIFORNIA

Los Angeles

Complex Microparticle Fabrication Using Optical Transient Liquid Molding and Cell Microcarriers

A dissertation submitted in partial satisfaction of the

requirements for the degree Doctor of Philosophy

in Mechanical Engineering

by

Chueh-Yu Wu

2016

ABSTRACT OF THE DISSERTATION

Complex Microparticle Fabrication Using Optical Transient Liquid Molding and Cell Microcarriers

by

Chueh-Yu Wu

Doctor of Philosophy in Mechanical Engineering

University of California, Los Angeles, 2016

Professor Dino Di Carlo, Co-Chair

Professor Pei-Yu Chiou, Co-Chair

There is need of applications of microparticles in various fields including tissue engineering, biosensing, photonic crystal, and drug delivery. It has been proven that porosity control using microparticles enhances wound healing while anisotropically-shaped microparticles are utilized for different types of Lab-on-a-Chip technologies. Ability of 3D shaping in microparticle fabrication plays a crucial role to not only improve the performance of current technologies but also create novel applications. Conventionally microparticles are fabricated using droplet generator, 3D printing, and stop flow lithography. However, it is challenging for droplet generator to produce asymmetric microparticles as 3D printing generates designed structure in a relatively slow speed. Stop flow lithography is operated in an intermediate speed to create 2D-extruded microparticles. 3D shaping microparticles in high throughput manner is highly demanded and promising for next-generation microparticle systems. In this dissertation, we briefly discuss on current microfluidics-assisted microparticle fabrications and applications, show our ability to control flow shape of photo-crosslinkable polymer

precursor in the out-of-plane direction using inertial flow engineering, demonstrate a novel manufacturing system of 3D-shaped microparticle based on inertial flow engineering, and present an innovative cell microcarriers synthesized using high throughput version of the system for advancing cellular studies. First, we provide three cases of microparticle fabrications and applications to show the significance of "*microfluidically-fabricated materials"* in the modern bioengineering fields. Secondly, we create *"fundamental inertial flow transformations"* of a flow stream in a co-flow experimentally and theoretically, showing that inertial flow engineering can generate increased complexity and asymmetry on micro-scale photolinkable polymer precursor. Third, *"optical transient liquid molding"* is introduced to be the core of a novel manufacturing system, which generates microparticles with shape of intersection of two 2D patterns by engineering inertial flows of photo-crosslinkable polymer precursor. Finally, we designed, manufactured, and characterized *"cell microcarriers"* with shape of intersection of a dumbbell and a slit with notches. We further develop a new version of optical transient liquid molding with high production rate for repeated biological experiments. The microcarrier system is demonstrated to be an innovative cell-culture platform, where the high-speed cell imaging and analysis can be achieved without bringing cells away from adherent status. To sum up, the integration of optical transient liquid molding and inertial flow engineering creates a new domain of microparticles with complexly asymmetrical shape, allowing wide applications including a new paradigm of cell culture using cell microcarriers.

The dissertation of Chueh-Yu Wu is approved

Chang-Jin Kim

Jeffery Eldredge

Pei-Yu Chiou, Committee Co-Chair

Dino Di Carlo, Committee Co-Chair

University of California, Los Angeles

2016

DEDICATION

Humbly dedicated to:

Mom and dad

Most beautiful wife, Jia-Yun (Sophia) Hsu

Table of Contents

Acknowledgements

Chapter 1

Research highlights: microfluidically-fabricated materials has been reprinted with minor adaptations with permission from (Jaekyung Koh, Chueh-Yu Wu, Harsha Kittur and Dino Di Carlo (2015) Research highlights: microfluidically-fabricated materials. *Lab on a Chip*, 15, 3818-3821.) Copyright (2015) Royal Society of Chemistry, USA. Professor Dino Di Carlo is the principal investigator of this work.

Chapter 2

Micropillar sequence designs for fundamental inertial flow transformations has been reprinted with minor adaptations with permission from (Daniel Stoecklein, Chueh-Yu Wu (Co-First Author), Keegan Owsley, Yu Xie, Dino Di Carlo and Baskar Ganapathysubramanian (2014) Micropillar sequence designs for fundamental inertial flow transformations. *Lab on a Chip*, 14, 4197-4204.) Copyright (2014) Royal Society of Chemistry, USA. Professor Dino Di Carlo is the principal investigator of this work.

Chapter 3

Rapid Software-Based Design and Optical Transient Liquid Molding of Microparticles has been reprinted with minor adaptations with permission from (Chueh-Yu Wu, Keegan Owsley, and Dino Di Carlo (2015) Rapid Software-Based Design and Optical Transient Liquid Molding of Microparticles. *Advanced Materials*, 27, 7970-7978.) Copyright (2015)

WILEY-VCH Verlag GmbH & Co. KGaA, 69469 Weinheim, Germany. Professor Dino Di Carlo is the principal investigator of this work.

Chapter 4

3D Microcarriers for Adherent Cell Culture and Analysis is a version of work in progress for publication by Chueh-Yu Wu, Daniel Stoecklein, Aditya Kommajosula, Keegan Owsley, Baskar Ganapathysubramanian, and Dino Di Carlo. Professor Dino Di Carlo is the principal investigator of this work.

VITA

EDUCATION

NATIONAL TAIWAN UNIVERSITY (NTU) Taipei, Taiwan

M.S. Institution of Applied Mechanics (IAM) **09/2005 – 07/2007**

B.S. Mechanical Engineering **09/2001 – 07/2005**

MAJOR PUBLICATIONS

Journals:

1. J. Kim, J. Lee, **C.-Y. Wu**, S. Nam, D. Di Carlo, and W. Lee, "Inertial focusing in non-rectangular cross-section microchannels and manipulation of accessible focusing positions," *Lab Chip,* Vol. 16, Issue 6, pp. 935-1090, Mar. 2016. (featured as the front cover image).
2. D. Stoecklein, **C.-Y. Wu**, D. Kim, D Di Carlo, and B. Ganapathysubramanian, "Optimization of micropillar sequences for fluid flow sculpting," *Physics of Fluids*, vol. 28, 012003, 2016.
3. **C.-Y. Wu**, K. Owsley, and D. Di Carlo, "Rapid Software-Based Design and Optical Transient Liquid Molding of Microparticles," *Adv. Mater.*, vol. 27, Issue 48, pp. 7970–7978, Dec. 2015.
4. D. Stoecklein, **C.-Y. Wu**, K. Owsley, Y. Xie, D. Di Carlo, and B. Ganapathysubramanian, "Micropillar sequence designs for fundamental inertial flow transformations," *Lab Chip*, vol. 14, Issue 21, pp. 4197–4204, Jan. 2014. (Co-First Author, featured as one of Lab Chip 2014 Hot Articles).
5. J. K. Nunes, **C.-Y. Wu**, CY, H. Amini, K. Owsley, D. Di Carlo, and H. A. Stone, "Fabricating Shaped Microfibers with Inertial Microfluidics," *Adv. Mate.*, vol. 26, Issue 22, pp. 3712–3717, Jan. 2014.

Research Highlights:

1. J. Koh, **C.-Y. Wu**, H. Kittur, and D. Di Carlo, "Research Highlights: Microfluidically-Fabricated Materials," *Lab Chip,* vol. 15, Issue 19, pp. 3818-3821, 2015.
2. **C.-Y. Wu**, O. Adeyiga, J.Lin, and D. Di Carlo, "Research Highlights: Increasing Paper Possibilities," *Lab Chip,* vol. 14, Issue 17, pp. 3258-3261, 2014.

Conference and Symposium Proceedings:

1. **C.-Y. Wu**, D. Stoecklein, K. Owsley, A Kommajosula, B. Ganapathysubramanian, and D. Di Carlo, “3D Shaped Cell Microcarriers for Cell Culture, Manipulation, High-throughput Analysis, and Sorting of Adherent Cells,” accepted to the 6th Annual International SLAS(Society for Laboratory Automation and Screening) Conference and Exhibition 2017.
2. **C.-Y. Wu**, K. Owsley, A. J. Chung, and D. Di Carlo, “Software-Based Design and Fabrication of Complex 3D Shaped Microparticles,” *Proc. the 18th International Conference on Miniaturized Systems for Chemistry and Life Sciences (μTAS)*, San Antonio, TX, October, 26-30, 2014.
3. **C.-Y. Wu** and D. Di Carlo, “Micro-Particle Migration and Separation Induced by Complex Flow Profiles,” *Proc. the 18th International Conference on Miniaturized Systems for Chemistry and Life Sciences (μTAS)*, San Antonio, TX, October, 26-30, 2014.

Chapter 1 :

Research highlights: microfluidically-fabricated materials

Polymer particles with precise shapes or chemistries are finding unique uses in a variety of applications, including tissue engineering, drug delivery, barcoding, and diagnostic imaging. Microfluidic systems have been and are continuing to play a large role in enabling the precision synthesis of designer particles in a uniform manner. To expand the impact of these microfluidic-fabricated materials additional fundamental capabilities should still be developed. The capability to fabricate microparticles with complex three-dimensional shapes and increase the production rate of particles to an industrial scale will allow evaluation of shaped particles in a range of new applications to enhance biological, magnetic, optical, surface wetting, as well as other interfacial or mechanical properties of materials. Here we highlight work applying large collections of simple spherical microgels, with unique surface chemistry that allows in situ particle–particle annealing, to form microporous injectable scaffolds for accelerated tissue regeneration. We also report on two other techniques that are addressing the ability to create 3D-shaped microparticles by first sculpting a fluid precursor stream, and increasing the rate of production of particles using contact lithography to millions of particles per hour. The combination of these capabilities and the applications they will enable suggest a bright future for microfluidics in making the next materials.

Injectable microporous gels formed from microfluidically-generated building blocks. Injectable or flowable biomaterial scaffolds are uniquely suited to aid in tissue regeneration by molding to a wound site or allowing minimally-invasive application. Delivered as a liquid and polymerized in situ, previous injectable scaffolds possessed a fundamental trade-off between overall mechanical strength and porosity/degradability enabling tissue ingrowth. Highly-crosslinked scaffolds that can maintain a structural support often result in reduced cell migration and ingrowth. Generating micropores in a scaffold promotes cellular infiltration while separately modulating bulk material properties;(1) nonetheless these microporous scaffolds generated using leaching methods must be manufactured ex situ.(2)

Griffin et al. tackled these issues with a bottom-up approach: creating a scaffold from microfluidically-fabricated building blocks.(3) Produced by a microfluidic water-in-oil emulsion method (Fig. 1a), uniform microsphere scaffold building blocks are polymerized, collected and brought into an aqueous solution where they are subsequently injected and annealed to one another enzymatically forming a Microporous Annealed Particle (MAP) gel (Fig. 1b and c). Micropores form as the network of void spaces between the covalently linked spherical gel particles. These building blocks are composed of a synthetic hydrogel mesh of multi-armed poly(ethylene) glycol-vinyl sulfone (PEG-VS) backbone decorated with cell-adhesive peptide (RGD), protease substrate crosslinkers, and two transglutaminase peptide substrates (K and Q). Via crosslinking of K and Q peptides by thrombin-activated Factor

XIII, an enzyme responsible for blood clotting, these neighboring blocks dynamically form the MAP scaffold in situ with a seamless interface (Fig. 1d and e).

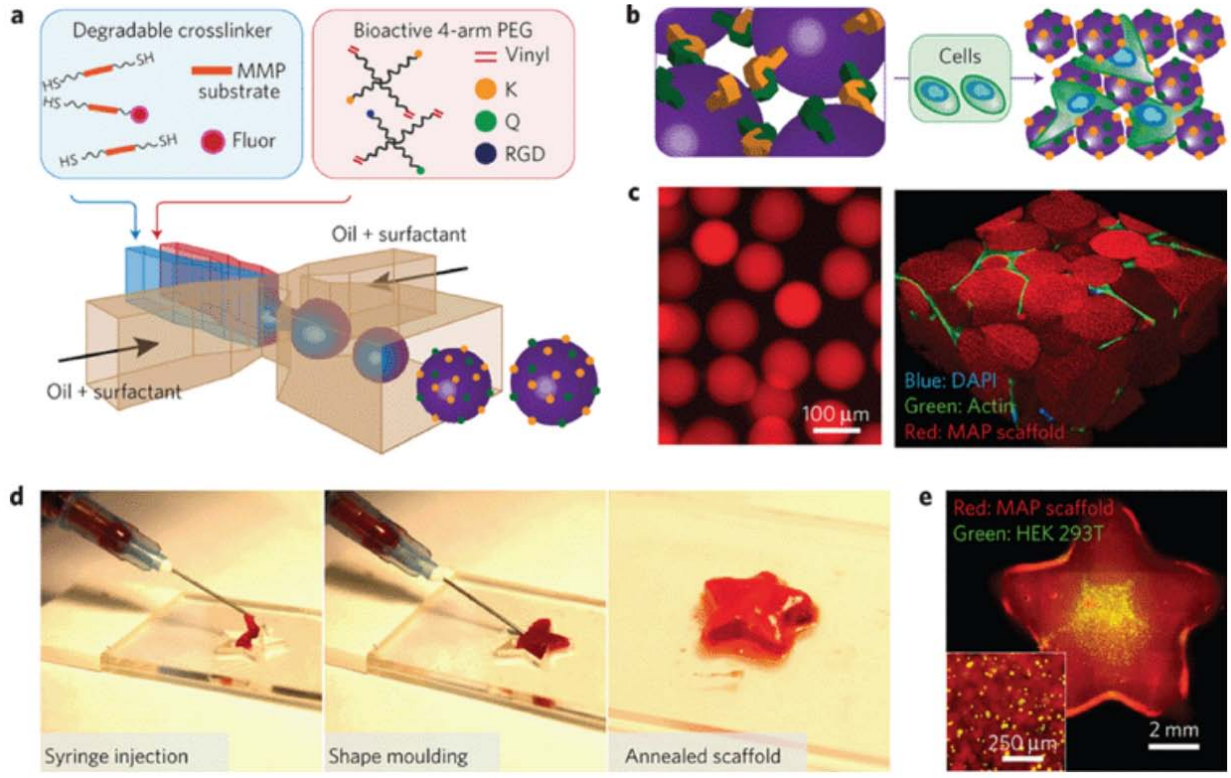

Fig. 1 Microfluidic generation of microsphere hydrogel building blocks for the creation of microporous annealed particle (MAP) scaffolds. (a) Scheme illustrating microgel formation using a microfluidic water-in-oil emulsion system. A pre-gel and crosslinker solution are segmented into monodisperse droplets followed by in-droplet mixing and crosslinking via Michael addition. (b) Microgels are purified into an aqueous solution and annealed using FXIIIa into a microporous scaffold, either in the presence of cells or as a pure scaffold. (c) Fluorescent images showing purified microgel building blocks (left) and a subsequent cell-laden MAP scaffold (right). (d) MAP scaffolds are mouldable to macroscale shapes, and can be injected to form complex shapes that are maintained after annealing. (e) This process can be performed in the presence of live cells. Reprinted with permission from Macmillan Publishers Ltd: Nature Materials. Griffin et al., Nat. Mater., 2015, 14, copyright 2015.

The chemical and physical properties of the scaffold can be tailored through microfluidic fabrication. The microporosity of the scaffold was modulated by the size of building blocks, which the authors precisely controlled with flow rate and geometry of the microfluidic device. The manipulation of storage moduli was achieved by varying PEG weight percentages and crosslinker stoichiometries, which were introduced into two separate inlet channels within the microfluidic device and only mixed once a droplet was formed. As a result, the moduli spans the stiffness regime necessary for mammalian soft tissue mimetics. In addition, the degradation of the scaffold was determined by the combination of microporosity and physical properties of the MAP gels.

The authors first demonstrated that cells could be seeded directly within the MAP gels prior to annealing, and following annealing extensive three-dimensional cellular networks rapidly formed for three human cell lines. They observed that cell networks increased in size and complexity through the entirety of the experiment and growth rate and cellular network formation greatly exceeded identical conditions with a non-porous gel. Furthermore, they were able to deliver the microgel building blocks directly to a wound site in murine skin by syringe injection, and found that the annealed MAP scaffold accelerated wound closure compared to control conditions or non-annealed scaffold by host-cell recruitment through microscale porosity. These results clearly support that the MAP scaffold prompts *in vitro* and *in vivo* cell spreading and migration as well as bulk tissue integration.

An important point is that imperfect self-assembly of the microgel building blocks leads to a robust formation of a porous scaffold, solving many issues with other bottom-up biomaterial approaches. Beyond wound healing, microfluidic-control over the building block generation provides a new bottom-up framework in tissue engineering scaffold fabrication; the self-assembled scaffold in situ combines the benefits of injectability, microporosity and modularity. Further increases in the production rate of microgel particles will be an important point to address in the future. Overall, this novel scaffold/gel should be able to improve tissue regeneration, organ-on-a-chip technologies, as well as stimulating clinical research and applications in wound healing.

Optofluidic fabrication of complex 3D particles using inertial flow sculpting. Particles with complex three-dimensional (3D) morphologies can offer unique functionalities, such as behavior under electrical stimulation, tighter packing density, and new optical characteristics, making them applicable to structural materials, photonics, and drug delivery. However, current manufacturing processes are limited in speed, resolution, and complexity of fabrication. Complex geometries can be produced using a wide range of materials with 3D printers, but at the cost of slow printing processes and low resolution. Injection molding techniques have similar advantages, but are limited to the shapes that can be produced with a mold.

In microfluidics, stop flow lithography (SFL) and optofluidic maskless lithography (OFML) can polymerize high-resolution 3D particles continuously by illuminating ultraviolet (UV) light on a static UV reactive fluid, but shapes have been mostly limited to 2D extrusions of the mask. Based on these principles, Paulsen, et al. have developed a new optofluidic fabrication method that relies on two sequential steps: (i) highly controllable inertial flow shaping in microfluidic channels(4) and (ii) UV photopolymerization of the shaped fluid stream.(5)

The optofluidic device uses two sheath fluid streams of poly(ethylene glycol) diacrylate (PEG-DA) from the side channels, sandwiching a photosensitive core fluid stream, PEG-DA with photoinitiator 2,2-dimethoxy-2-phenylacetophenone (DMPA). The first step requires permanent deformations in the central fluid stream, generated by strategically placed perturbation pillars that induce secondary flows (Fig. 2a). This requires the presence of slight inertial effects at the microscale where fluid fields irreversibly deform in a laminar flow regime (i.e. Reynolds number, Re = 10–100). This flow field deformation is enhanced with the addition of more pillars in the downstream direction. Numerical analysis shows that a series of side pillars can transform the side view velocity field of the center stream from a rectangle to an I shape at Re = 14.58, while little change is observed in Stokes flow (Re = 0.04). This flow shaping was demonstrated experimentally using co-flows of non-fluorescent sheath side streams with a Rhodamine B dyed core fluid stream, yielding significantly greater distribution of fluorescence intensity across the width of the stream for the inertial flow case. The second step of the fabrication process is similar to the aforementioned SFL technique.

Downstream to the pillars, the shaped core fluid is exposed to UV light that is illuminated against a pre-designed photomask (Fig. 2a).

To start, the authors demonstrate the ability to shape fluid with central pillars vs. side pillars by masking with a simple slit-shaped photomask, exposing the shaped fluid after each pillar (Fig. 2b). In addition to pillar number and configuration, variation of Re was tested. Higher Re is characteristic of higher inertia, generally, leading to greater perturbations. Finally, as proof of concept, complex 3D particles were generated by combining flow stream sculpting and UV light shaped by a photomask (Fig. 2c).

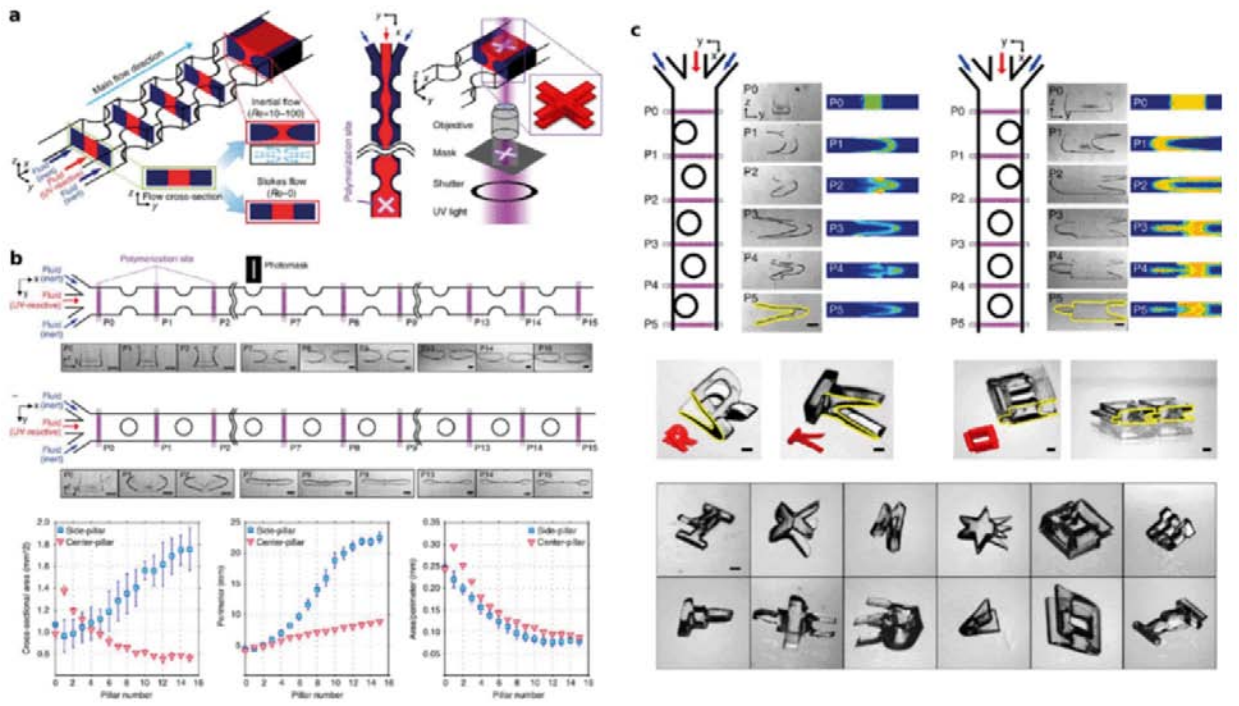

Fig. 2 Generation of complex 3D particle using optofluidics. (a) The flow field core photosensitive stream is inertially shaped with pillar obstacles, and is subsequently exposed to UV light against a patterned mask. (b) Keeping Reynolds number and photomask shape constant, the pillar arrangement can stretch or compress the cross-sectional area of the stream. (c) Unique pillar arrangements can yield predictable flow fields in fluid dynamic simulations which can then be applied with the photomask of choice to produce high-resolution intricate particles. All images were adapted from Paulsen et al. with permission.(5)

In this work, the authors have demonstrated a high-throughput, inexpensive, continuous flow system for generating complex 3D particles in a systematic manner, overcoming the speed and resolution limitations of 3D printers, and the complexity limitation of other microfluidics techniques. One limitation of this work may be the non-intuitive translation of pillar arrangement to projected inertial flow field. Further, a better understanding of the space of shaped particles that can be fabricated is needed and how particle size

can be scaled down.(6) Nevertheless, the work should open up whole new classes of microparticles that should enable innovations across a variety of fields.

Scaling microparticle production with contact flow lithography. A challenge for microfluidic material fabrication, including the techniques discussed above, is scaling to higher production rates. Current technologies, for example, droplet-based microfluidic techniques and imprint lithography, face challenges to manufacture particles with non-spherical shapes in a high-throughput manner. Various approaches to flow-through photolithography have been developed to automate and scale up anisotropic microparticle synthesis. However, there is a bottleneck in particle synthesis rate because the illumination area with a lens-based setup is severely limited.

Le Goff et al. report a contact photolithography system to achieve an ultrahigh production rate of particle synthesis, about 10^6 particles per hour.(7) In the system, collimated illumination, generated by a high power UV light-emitting diode (LED), exposes eight channels (950 µm × 10 mm) simultaneously through a photomask in direct contact with the microfluidic device. The system produced ~6000 100 µm sized particles for each UV exposure (see Fig. 3a and b) with a cycle time of about 7.5 s between exposures. The authors show agreement of the qualitative shape and highly uniform size (CV = 3.3%) demonstrating the reproducibility of the approach (see Fig. 3c). As an add-on value of the instrument, the authors demonstrated the ability to pattern one- or two-layer hydrogel microstructures across 23 mm circular areas. In sum,

particle synthesis using contact flow lithography enables many fundamental studies which require large numbers of particles and paves the way to create microstructures at an industrial scale, potentially benefiting the fields of rheology, drug formulation, biosensing, cell culture, and beyond.

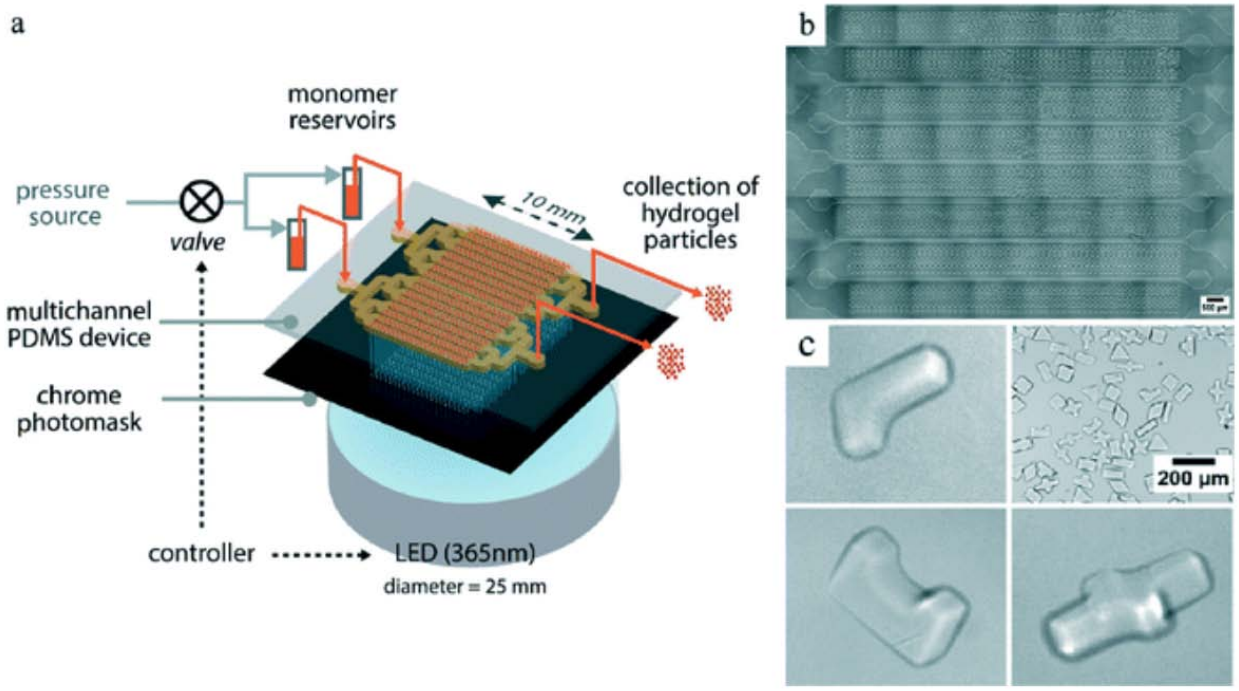

Fig. 3 Contact flow lithography over large areas. (a) Schematic of the experimental setup for contact flow lithography. (b) Images of fabricated particles in eight channels after one UV exposure. (c) PEGDA hydrogel particles collected outside of the fabrication system. All images were adapted from Le Goff et al. with permission.(7)

Bibliography

[1] M. Okamoto and B. John, Prog. Polym. Sci., 2013, 38, 1487–1503.

[2] S. A. Bencherif, R. W. Sands, D. Bhatta, P. Arany, C. S. Verbeke, D. A. Edwards and D. J. Mooney, Proc. Natl. Acad. Sci. U. S. A., 2012, 109, 19590–19595.

[3] D. R. Griffin, W. M. Weaver, P. O. Scumpia, D. Di Carlo and T. Segura, Nat. Mater., 2015, 14, 737–744.

[4] H. Amini, E. Sollier, M. Masaeli, Y. Xie, B. Ganapathysubramanian, H. A. Stone and D. Di Carlo, Nat. Commun., 2013, 4, 1826.

[5] K. S. Paulsen, D. Di Carlo and A. J. Chung, Nat. Commun., 2015, 6, 6976.

[6] D. Stoecklein, C.-Y. Wu, K. Owsley, Y. Xie, D. Di Carlo and B. Ganapathysubramanian, Lab Chip, 2014, 14, 4197–4204.

[7] G. C. Le Goff, J. Lee, A. Gupta, W. A. Hill and P. S. Doyle, Adv. Sci., 2015.

There are many technologies developed for microparticle fabrication, including droplet generator, 3D printing, and stop flow lithography, which was discussed in the Highlight paper. However, droplet generator only creates symmetrical microparticles while 3D printing suffers from producing objects in a low speed. Stop flow lithography can fabricate complex microparticles in a moderate speed but the shape is still restricted to 2D-extruded objects. For these conventional technologies, the key challenge is to efficiently generate pattern or structure with liquid polymer precursor in the out-of-plane direction. To solve the problem, we discovered the capability of “inertial flow engineering” in the following paper, “Micropillar sequence designs for fundamental inertial flow transformation,” to manipulate the shape of flow in the lateral (out0of-plane) direction.

Chapter 2 :

Micropillar sequence designs for fundamental inertial flow transformations

Abstract

The ability to control the shape of a flow in a passive microfluidic device enables potential applications in chemical reaction control, particle separations, and complex material fabrication. Recent work has demonstrated the concept of sculpting fluid streams in a microchannel using a set of pillars or other structures that individually deform a flow in a predictable pre-computed manner. These individual pillars are then placed in a defined sequence within the channel to yield the composition of the individual flow deformations - and ultimately complex user defined flow shapes. In this way, an elegant mathematical operation can yield the final flow shape for a sequence without experiment or additional numerical simulation. Although these approaches allow for programming complex flow shapes without understanding the detailed fluid mechanics, the design of an arbitrary flow shape of interest remains difficult, requiring significant design iteration. The development of intuitive basic operations (i.e. higher level functions that consist of combinations of obstacles) that act on the flow field to create a basis for more complex transformations would be useful in systematically achieving a desired flow shape. Here, we show eight transformations that could serve as a partial basis for more complex transformations. We initially used an in-house, freely available custom software (uFlow) which allowed us to arrive at these transformations that include making a fluid stream concave and convex, tilting, stretching, splitting,

adding a vertex, shifting, and encapsulating another flow stream. The pillar sequences corresponding to these transformations were subsequently fabricated and optically analyzed using confocal imaging - yielding close agreement with uFlow-predicted shapes. We performed topological analysis on each transformation, characterizing potential sequences leading to these outputs and trends associated with changing diameter and placement of the pillars. We classify operations into four sets of sequence-building concatenations: stacking, recursion, mirroring, and shaping. The developed basis should help in the design of microfluidic systems that have a phenomenal variety of applications, such as optofluidic lensing, enhanced heat transfer, or new polymer fiber design.

1. Introduction

The ability to control the cross-sectional shape of a fluid stream is enabling for a variety of microfluidic applications, from optimizing mixing for reactions and heat transfer (1) to developing tunable optical component such as fluid lenses (2), to fabricating shaped polymer fibers(3). The most common methods by which fluid parcels have been diverted across a channel cross-section to shape a stream make use of asymmetric structured channels (e.g. grooves, chevrons) in Stokes flow4 or curved channels with finite inertia(1,5,6). Grooved channels have been widely used to mix flows(7) and more recently combinations of grooves have been combined to shape flows(8) in a programmable manner.

Fluid inertia also allows for the cross-stream motion of fluid parcels in curving or structured channels. Inertial fluid flow ($1 < Re < 100$, where the Reynolds number, $Re = {}^{\rho UDH}/\mu$, is the ratio of inertial to viscous forces in the flow, with fluid density ρ, viscosity μ, downstream velocity U, and hydraulic diameter D_H) has recently seen increased interest in the microfluidics community, with various strategies for manipulating particles emerging from equilibrium inertial focusing effects and the action of inertial lift forces on particles(6,9). Fluid streams within a channel can also be deformed by the presence of particles(10), curvature(1), or channel structure(11). Beebe et al employed a serpentine channel design which efficiently used chaotic advection for mixing fluids(5). This most common approach used Dean flows, which are induced secondary flows through curved channels, to deform the flow field and increase interfacial area for mixing. Dean flow can also act in superposition with inertial lift forces to reduce the number of stable particle focusing positions(6). A remarkable example of fluid flow engineering via Dean flow was the creation of a tunable optofluidic lens(2). But Dean flow is limited in its ability to precisely deform a particular region of the fluid - that is, the entire flow cross-section is manipulated. Particle-induced convection and Dean flow-based schemes - while useful for mixing - are difficult to adapt to arbitrary flow sculpting. However, recent developments in geometry induced secondary flows under finite inertia conditions show promise for novel strategies in microfluid engineering with local flow stream perturbations(11).

The inertial flow around a cylindrical pillar yields secondary flows within a channel cross-section that are localized to the pillar location. The flow deformation around a simple geometry in this inertial regime has been only recently investigated in

microfluidic systems, due to the general assumption of Stokes flow creating fore-aft symmetry in flow deformations around an object6. Experimental work has made use of flow separation and recirculations that form downstream of obstacles, where the fore-aft symmetry is broken in inertial flow around a geometry placed in the cross section of the fluid stream(1,12). More recently, microscale cylinders (pillars) have been used to induce secondary flow (separate from the flow separation) and this has been used in tandem with inertial focusing in order to reposition particle streams at highthroughput(13). A single cylindrical pillar at a variety of lateral positions in a microchannel has been found to induce a set of local fundamental deformations in inertial flow around each pillar(11). One notable aspect of the inertial flow deformation past a micropillar is the saturation of the turning motion of the flow within a limited distance downstream (<~4 pillar diameters), which leads to the idea of 'programmability' using pre-computed advection maps for each pillar that are sequentially combined.

With appropriate inter-pillar spacing, pillars placed sequentially in a microfluidic channel can be used to sculpt the fluid into complex new configurations with little new computation(11). Useful subsequences can be labelled as functions, which can act on fluids alone or concatenate in order to tailor the flow as desired. These 'pillar programs' can open up an extensive library of associated net deformations for future microfluidic applications, such as using shifted fluid streams to improve heat transfer from local hotspots, creating new methods of cell sorting in bio-medical diagnostic 'lab-on-a-chip' devices, enhancing reactions at the interface between fluids by increasing surface area of streams, or changing the cross-section shape of polymer precursors for novel material design3. The complicated phase space on offer per micropillar was initially

described through dimensional analysis using three non-dimensional groups: the Reynolds number, the channel aspect ratio h=w, and normalized pillar diameter D=w, where h, w, and D are the channel height, width, and pillar diameter. A dataset of 12,400 transformations with varying pillar diameter, offset, channel height, and flow Reynolds number was generated through distributed HPC resources by Diaz-Montes et al (14). Changing the pillar position and diameter was observed to have a tremendous effect on the fluid transformation with rich variety of shapes, but the vast number of permutations for sequences from this large dataset made for a daunting phase space of pillar programs. Therefore, a reduced, discretized framework was created for a preliminary foray into understanding what is possible with pillar programming. In order to quickly explore the potential operations allowed by this new method of microfluid engineering, we introduce a lightweight program (uFlow, www.biomicrofluidics.com/software.php) that uses a database of high precision 3D simulations based on single-pillar deformations. We first utilize this easily extensible program to develop intuition with the most fundamental transformations (one to three pillars per sequence), which we eventually combine to design more complex, hierarchically designed transformations. This facilitates rapid investigation of pillar programs without requiring access to high performance computational power. A set of eight fluid transformations, chosen for potential applications in microfluidics, are initially identified as target transformations. This first set of functions helps to illustrate the impact of pillar programming, in addition to signaling the potential complexity of a more complete library of programs. Upon obtaining these novel transformations through this software exploration, we validated the designs by fabricating microfluidic devices and

conducting confocal imaging. This work presents specific sequences used to create the target operations, along with some of the basic intuition, tools, and analysis that emerged from the process of finding and understanding these operations.

2. Objective

8 fundamental transformations were identified to be potentially useful in microfluidic applications, and are illustrated in figure 1. Unless specified otherwise, all transformations will be acting on a fluid region of interest 1/5 the width of the channel, and spanning the entire height (figure 1(b)).

- '*Make Concave*' (figure 1(a-i)) and '*Make Convex*' (figure 1(a-ii)) give curvature to the fluid interface for potential microscale optofluidic applications, or as a basic tool for hierarchical design by collapsing or expanding the fluid at different sections.
- '*Tilt*' (figure 1(a-iii)) is among the most basic transformations, and could be utilized for minor deformations in hierarchical design, or as a simple folding mechanism for enhanced mixing.
- '*Stretch*' (figure 1(a-iv)) flattens the fluid region, and its ability to collapse the whole shape could be useful in program design, as many transformations will have weaker effects on the fluid elements near the microfluid channel walls. Control over the thickness of the fluid via *stretch* will aid more complex fiber design.
- '*Split*' (figure 1(a-v)) has applications for fiber design and could lead to simultaneous engineering of separate streams in the microfluid channel.
- '*Add Vertex*' (figure 1(a-vi)) stands apart from most of the transformations due to its sharp vertices at the midsection of the fluid. Such angles could help define a more

robust interlocking structure, or hint to more complex polygonal transformations.

- ‘*Shift*’ (figure 1(a-vii)) is a very powerful manipulation of the fluid flow, with potential to isolate and further engineer fluid regions of interest. A program that could laterally shift streams will be a boon to mixing, heat transfer, solution reactions, and other far-reaching applications.
- ‘*Encapsulate*’ (figure 1(a-viii)) seeks to envelope a fluid stream with the primary, central stream. It could be used to create a polymer sheath, induce coaxial solution reactions, or for general mixing applications.

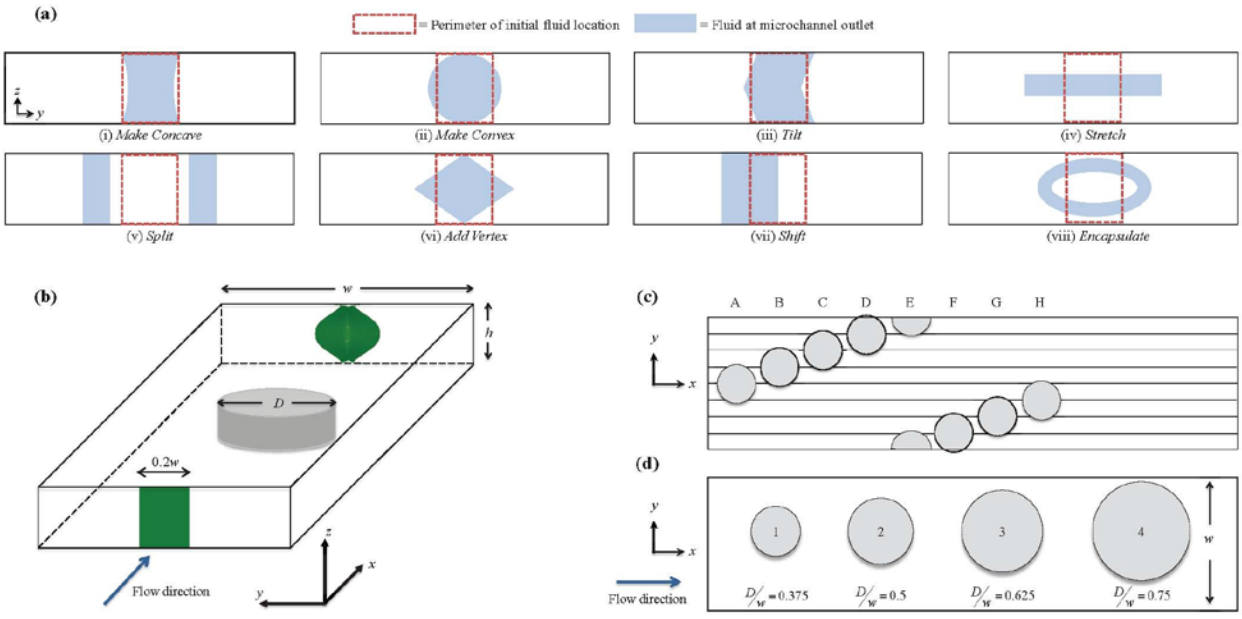

Fig. 1 (a) Objective transformations. (b) Schematic of microchannel, showing a cross-section of the fluid elements at the inlet (middle 20% being tracked), and a sample deformation induced by a single pillar at the center of the channel. (c) Discretized simulation scheme lettered indices for locations space 1/8*w* (A-H), and (d) pillar diameters shown with indices 1-4, labelled with true pillar diameter and drawn to scale.

3. Method

3.1 Computational

The phase space for this initial study is limited to manipulating the non-dimensional pillar diameter, $^{D}/w$, and lateral location, $^{y}/w$. The position was defined by eight equally spaced offsets in a microchannel ($^{h}/w$ = 0.25), while pillar diameters were restricted to $^{D}/w$ = 0.375, $^{D}/w$ = 0.5, $^{D}/w$ = 0.625, $^{D}/w$ = 0.75. The velocity field for each pillar case was computed by solving the Navier-Stokes equations using the finite element method, incorporating streamline-upwind/Petrov-Galerkin (SUPG) (15) and pressure-stabilizing/Petrov-Galerkin (PSPG) (16) terms to stabilize the numerical solution. No-slip boundary conditions are applied on the lateral walls and the surface of the pillar. Due to symmetry of the flow field, the simulation is only performed on the top half of the channel with a mirror boundary condition of velocity components on the centerline of the channel. We assume that the fluid is incompressible and at a steady state, and that the velocity profile is fully developed at the inlet. The pressure drop between the inlet and outlet is fixed and is determined to match the flow rate. The inlet velocity profile and pressure drop are calculated with the method used in (17), where the inlet velocity profile is predicted by solving the 2D cross-section flow with a guessed pressure gradient from the Hagen-Poisseuille law, and then corrected by linearly adjusting the pressure gradient to give the correct flow rate. For each configuration, fluid parcels were tracked through their respective velocity field to produce an advection map, which describes the displacement of each parcel as it travels down the channel. Stream deformation is characterized by marking those fluid parcels that belong to a stream of interest, and looking up the motion of those particles in the advection map. Advection

maps are concatenated by using a parcel's deformed location to lookup the displacement in the following map, and summing displacements down the pillar sequence. The result is a new advection map comprising of the net effect of the entire pillar sequence.

3.2 uFlow

A lightweight utility "uFlow" was created (and is freely available online) that composes advection maps in real-time using the graphical processor (GPU) available on most modern consumer computing hardware. The software presents a simple graphical user interface that allows the user to place pillars into a straight channel and mark regions of the flow using a pallette of colors. Feedback is provided immediately in the form of cross-sectional views of the fluid between each pillar and at the end of the channel.

In order to provide realtime feedback, uFlow takes advantage of some properties of advection maps that make them amenable to the highly parallelized computing provided by the GPU. Briefly, the pre-computed advection maps for each pillar are loaded as OpenGL floating point textures, with x, y, and z displacements stored in the blue, red, and green channels, respectively. A render-to-texture framebuffer object of the same size as the advection maps is created to store the output. A custom fragment shader is executed for each "pixel" in the framebuffer, corresponding to a single fluid parcel in the advection map. The fragment shader performs two fast texture lookups using the GPU's texture fetching hardware, and combines two advection maps into a single map corresponding to the net parcel displacement. The result is stored into a texture, and can be used as the input advection map for a subsequent pillar. In this way, the net displacement for each parcel is accumulated as it travels down the channel.

For visualization, a custom vertex shader performs a texture lookup into the advection map, and uses this information to deform particle locations. The deformed particles are rendered onto the user's screen, and optionally exported to a high-resolution png. This entire loop occurs in realtime on typical laptop hardware.

3.3 Fabrication

The microfluidic devices for verifying transformations were fabricated using conventional soft photolithography. The microchannels with sequence of pillars were designed to be 200 µm by 50 µm, and standard photolithography was utilized to produce corresponding mold from a silicon master spin-coated with KMPR 1050 (MicroChem Corp.). Sylgard 184 Elastomer Kit (Dow Corning Corporation) was used to replicate the polydimethylsiloxane (PDMS) devices from the mold. PDMS base was mixed with a curing agent with a ratio of 10:1, and poured into the molds placed in the petri dishes. The petri dishes were put in a vacuum to remove bubbles and then in an oven until fully cured. The PDMS devices were peeled from the mold and punched using a pin vise (Technical Innovations, Inc.) to create inlet and outlet holes. The PDMS device and a thin glass slide were activated by air plasma (Plasma Cleaner, Harrick Plasma) and bonded together to enclose the microchannel. To help visualizing the channel, Rhodamine B (Sigma-Aldrich) was infused into the channels to permeate the PDMS layer, and washed after one night.

3.4 Confocal Imaging

The confocal images were obtained using a Leica inverted SP1 confocal microscope at

the California NanoSystem Institute. For each transformation, the bonded microfluidic device was taped tightly on the stage of microscopy and its three inlets were connected to three syringes set on three separate syringe pumps (Harvard Apparatus PHD 2000) by PEEK tubing (Upchurch Scientific Product No. 1569). The middle syringe included fluorescent isothiocyanate dextran 500kDa (5 μM, Sigma-Aldrich) dissolved in deionized water to help with visualization of the deformed stream, and the other two were filled only with deionized water. The volume flow rate of each pump is proportional to area of the flow stream at the microchannel inlet, with a total volume flow rate of 150 μL/min. The images were taken perpendicular to the flow direction at a downstream location of at least four times the pillar diameter from the last pillar. Six images were taken and averaged to get a final image for each case to avoid random noise.

4. Results

Figure 2(a-h) shows pillar sequences found to engineer the fluid into each objective output (not shown to scale). There are two indices for each pillar (above the channel schematic and within the pillars). The naming convention for pillar program schematics is as follows: the lettered index above the figure represents the pillar's position in the channel, with eight possible positions (see figure 1(c)). The numbered index placed inside of the pillar denotes its diameter, with four numbers corresponding to four diameters: 1 = 0.375w, 2 = 0.5w, 3 = 0.625w, and 4 = 0.75w (see figure 1(d)). Re = 20 for all conditions, and the channel aspect ratio h/w = 0.25.

We divide the pillar programs into two categories: fundamental and hierarchically designed transformations. The fundamental transformations are created using simple

programs with three or fewer pillars, and can be leveraged in sequence in order to create the more complex hierarchically designed transformations.

5. Discussion

5.1 Pillar Sequence Concatenation

The exploration of pillar sequences and a subsequent search for target transformations was enabled by an understanding of how transformations can be used in sequence to appropriately sculptflow. Because of the deterministic mapping of fluid elements upstream to downstream of the pillar sequences, the sequences themselves can be 'concatenated' end to end to create more complex programs. We identified four classes of concatenation, presented in order of simplicity:

- stacking
- recursion
- mirroring
- shaping

Stacking operations simply repeat the location and diameter of the prior pillar exactly, as seen in figure 3(a). It is typically seen to create a more exaggerated transformation of the previous pillar. A recursive operation is like stacking, but instead of a single pillar, a subsequence of pillars is repeated, as seen in the first pillar program of figure 3(b-i). A sequence of two pillars at positions H and B is repeated, thereby eliciting a more

pronounced vertex on the left side of the midsection. Mirroring builds on recursion, except each location of the repeated subsequence is “mirrored” across the microchannel’s longitudinal centerline, as demonstrated in figure 3(b-ii). Mirroring can be useful creating symmetric transformations from asymmetric functions, allowing shapes to have more complex edges. A clear example of this is the overall *add vertex* transformation: mirroring is used to form vertices, while each pillar deformation is based on secondary flows that contain no obvious sharp angles. Finally, shaping is simply an arbitrary concatenation of any subsequence to a different one, provided it is not stacking, recursive, or mirroring. An example is seen in figure 3(b-iii), where the known effect of *make convex* is used to create the net shape of *add vertex*. Shaping is a critical tool for discovering new transformations by building on a foundation of fundamental operations, for the user can attempt to sculpt a fluid packet in a way defined by an operation already seen, thus further defining the hierarchy of pillar programming.

5.2 Analysis of *Make Concave*/*Make Convex*

Make concave is formed by a basis of two half-pillars at the channel wall of diameters D/w = {0.375,0.5,0.625} (figure 4). A diameter of 0.75w induces sharp corners in the fluid geometry, and is not effective in creating a smooth concave shape. Changing the pillar diameter changes the curvature of the fluid element, with a varying radius of curvature across the middle $1/3$ of the contour as plotted in figure 4(b). Note the change in behavior with pillar diameters larger than D/w = 0.375; the ‘longer’ sequences tended to force more fluid to the edges of the channel, and created a more linear contour at the

convex shape's midsection, thus increasing the radius of curvature for the majority of the shape. While it seems that the largest space to work while maintaining a truly convex shape is with D/w = 0.375, mass diffusion effects may be magnified by difficulty manufacturing smaller diameter pillars. Figure 2(a) shows a poor reproduction of the numerical prediction even with the modest pillar size of D/w = 0.625, suggesting the need for incorporating a diffusion model into the computational framework.

Make convex is a qualitative counterpart in output and program to *make concave*, and primarily uses a single pillar with diameters D/w = {0.375,0.5,0.625}. D/w = 0.75 results in an irregular hexagon at the output and therefore not satisfying the target operation requirements. Tunable convex and concave fluid shapes could provide a straight-channel alternative to Deanflow for the application of optofluidics, in addition to novel polymer shapes, of fluid focusing techniques. The average change in radius of curvature per number of pillars of similar diameter used is shown in figure 4(d). Again, it should be noted that the curvature shown is an average of the curvature for the middle $1/3$ of the contour, as the profile is parabolic in nature, and becomes linear near the edge.

5.3 Analysis of *Stretch*/*Split*

The *stretch* transformation is accomplished by placing pillars on the center position of the channel. Though larger diameters can stretch fluid element more rapidly - therefore requiring fewer pillars for a desired output -it is possible to overshoot the goal of a stretching deformation and move into the *split* transformation. *Stretch* is another

example of how a transformation can be found through different pillar sequences. Figure 5(a) shows how a 5 pillar sequence with pillars of $^{D}/_{w}$ = 0.5 (figure 5(a-i)) can be effectively recreated using a 3 pillar sequence with pillars of $^{D}/_{w}$ = 0.625 (figure 5(a-ii)). Attempting to create this same transformation via 3 pillar sequence with $^{D}/_{w}$ = 0.75 results in the beginning of the *split* transformation (figure 5(a-iii)), but still meets the goal of the *stretch* transformation. The variety of sequences for similar transformations shows the richness of the phase space, in addition to emphasizing the future need for numerically optimizing for minimal pillar sequences in order to mitigate diffusion effects. Figure 5(b) illustrates the effect of increasing the pillar diameter on the change in fluid width, per number of pillars in the sequence. The *split* transformation (figure 2(e)) is an example of how pillar program recursion can produce an entirely new operation. Placing at least seven pillars of $^{D}/_{w}$ = 0.625 results in a separation of the fluid element into two roughly circular elements with diminishing tails on either side of the channel. Adding an eighth pillar begins to distort the separated elements until they begin to wrap back into the center of the channel, beginning a potential mixing scheme.

5.4 Analysis of *Tilt*

The *tilt* program shown in figure 2(c) creates a 38 $^{\circ}$ tilt, with an internal angle of 104 $^{\circ}$. *Tilt* forms the basis for several hierarchical operations, but there are very few ways to create *tilt* with the reduced framework. The sequence uses pillar diameters of $^{D}/_{w}$ = 0.375, but moving to $^{D}/_{w}$ = 0.5 removes the vertex in the transformation. Similarly,

moving outward in lateral placement also removes the vertex. This motivates the future analysis of a larger dataset with fine-grained pillar diameters and locations, which would allow for sensitivity analysis to determine the degree of error allowed in manufacturing pillar sequences.

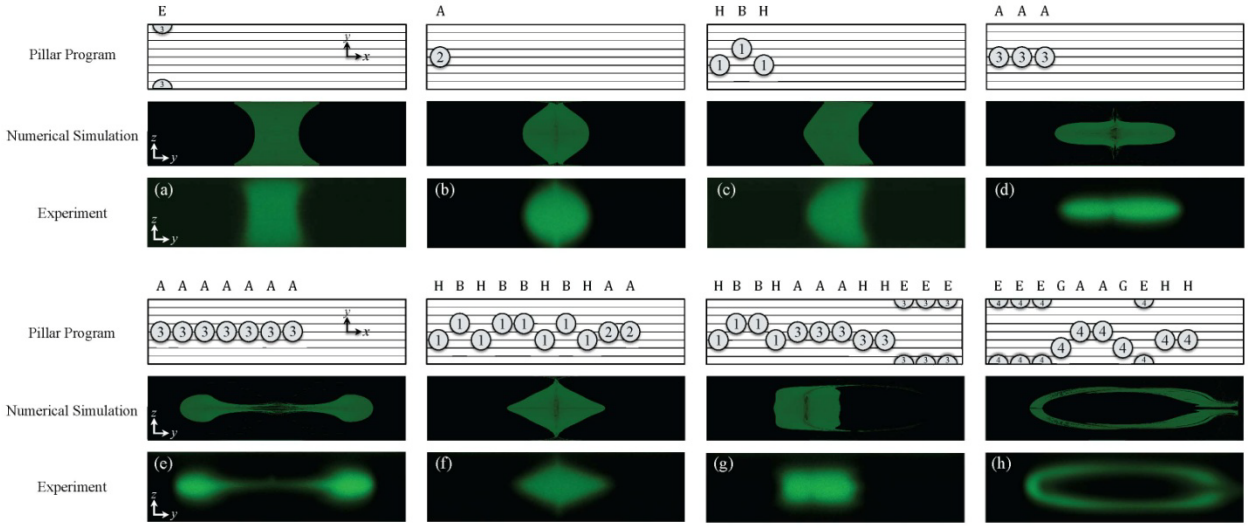

Fig. 2 Fundamental transformations '*Make Concave*' (a), '*Make Convex*' (b), '*Tilt*' (c), '*Stretch*' (d), and Hierarchical transformations '*Split*' (e), '*Add Vertex*' (f), '*Shift*' (g) and '*Encapsulate*' (h). The figures show the pillar sequence schematic on top, the numerical prediction as an output from uFlow in the middle, and the experimental validation on the bottom.

5.5 Analysis of *Add Vertex*

Different programs were found to arrive at the add vertex transformation, but the sequence shown in figure 3(b-iii) contains the sharpest vertices. There are two primary components to this sequence: the creation of an irregular decagon with vertices protruding at the channel centerline, and the use of *the make* convex program to complete the final shape. The irregular decagon is formed by mirroring a modified 38° tilt sequence that adds a vertex to one side of the fluid structure, which results in two vertices symmetric about the channel's y-axis, as shown in figure 3(b-ii). The *make*

convex program, 2 pillars with D/w = 0.5, is concatenated onto the previous eight pillars to finish the transformation. An alternate route is to decrease the mirrored sequence from four to two pillars. This creates a 5 pillar program, but alters the output edges to become more smooth and convex (see figure 6(b)).

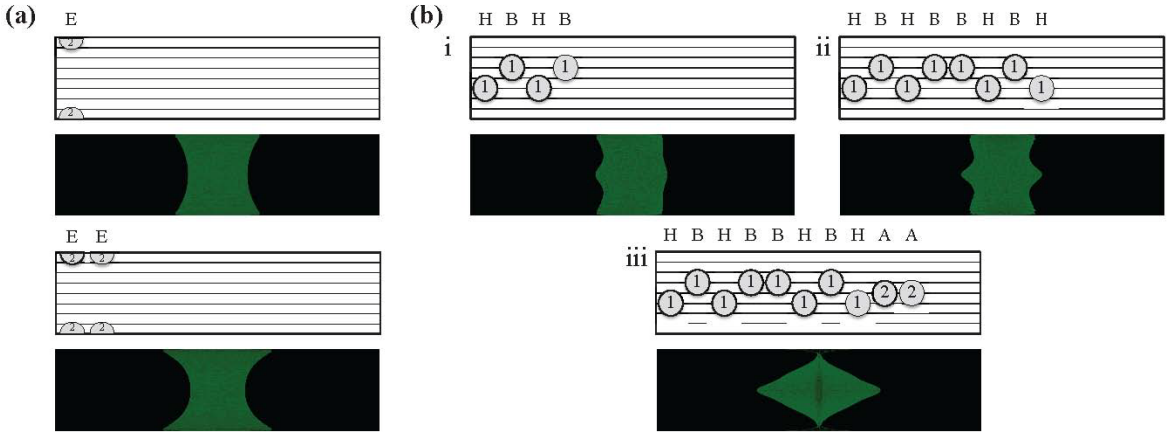

Fig. 3 (a) Stacking demonstration with *make concave*. (b) Creation of *add vertex* via recursion (i), mirroring (ii), and shaping (iii).

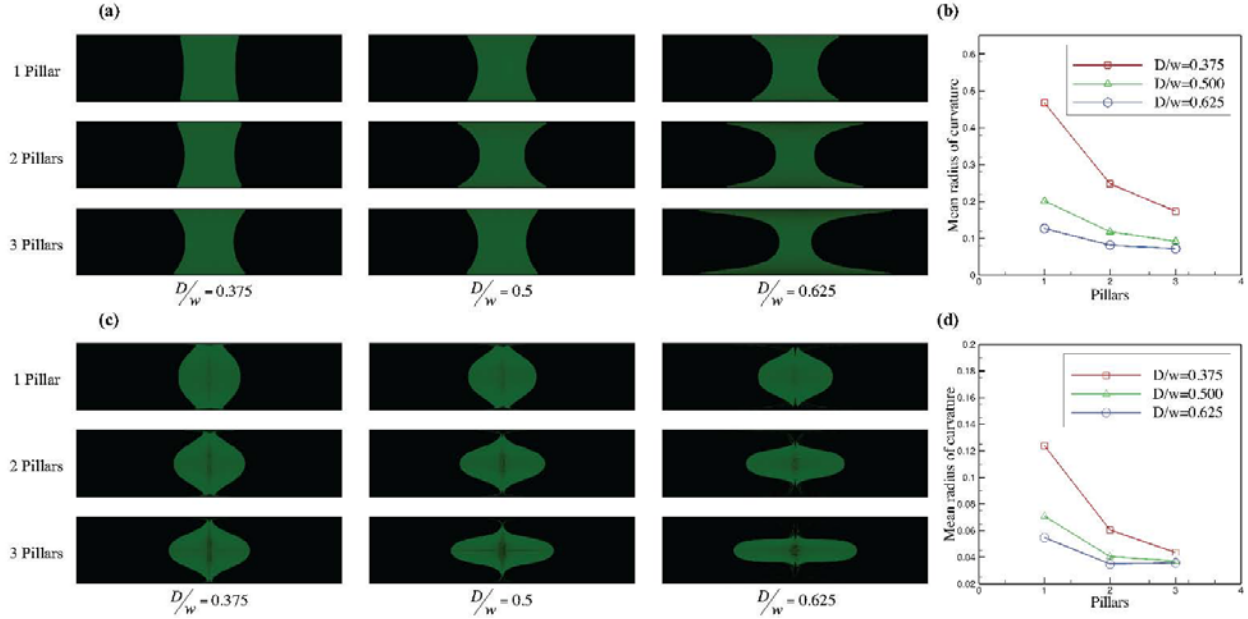

Fig. 4 Illustrations of (a) *make concave* and (c) *make convex* per pillar type through 3 pillars, and changes in mean radius of curvature vs. number of similar pillars in sequence for (b) the *make concave* and (d) *make convex* operations.

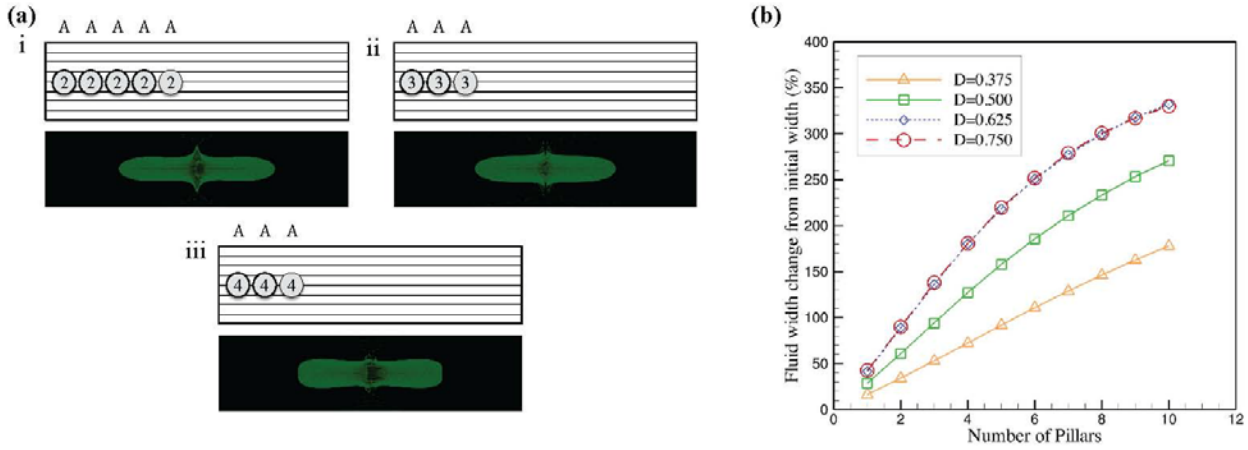

Fig. 5 (a) Multiple routes to similar *stretch* transformations. Note that three pillars of *D*/*w* = 0.625 achieves roughly the same output as five pillars of *D*/*w* = 0.5. Moving to a *D*/*w* = 0.75 begins the *split* transformation sooner, in addition to flattened ends. (b) (Please view in color) The effect of changing diameter and increasing numbers of central pillars on the stretched width of the central fluid element. Note that *D*/*w* = 0.75 and *D* = 0.625 are functionally identical for this effect.

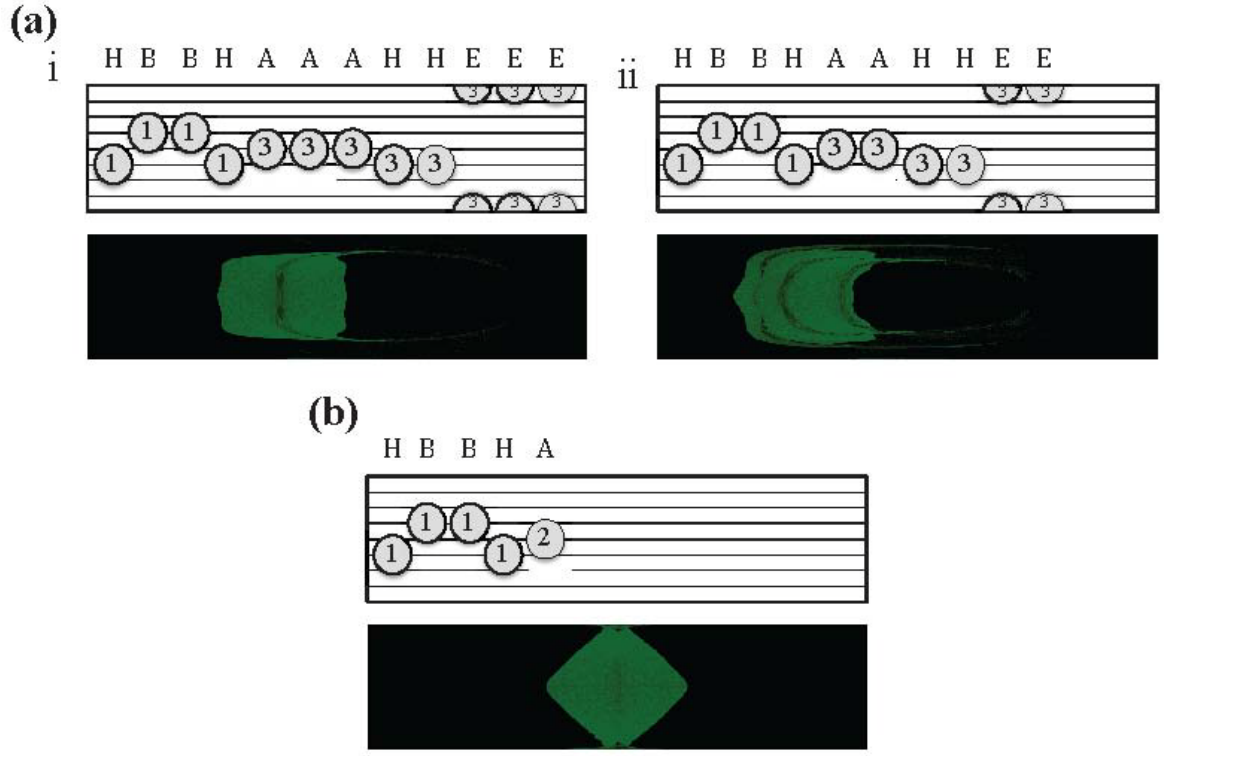

Fig. 6 (a) 10% *shift* (i) and 20% *shift* (ii). Note that the program for 20% *shift* is concatenated onto the 10% sequence, for a total of 22 pillars. (b) Alternative 5 pillar approach to *add vertex*, demonstrating the same recursion/mirroring/shaping methods as the 10 pillar version.

5.6 Analysis of *Shift*

The initial strategy for shifting a fluid element was to begin with a *stretch* program and then force the fluid to either side of the channel with pillars to the left or right of the centerline. Thin 'tails' are formed in the most basic *shift* sequences, as seen in figure 6(a-i). These tails are a natural consequence of the secondary flow at the center of the channel, which -coupled with the no-slip boundary condition -results in an incomplete pinching effect at the wall/fluid interface. To marginalize this effect, the *add vertex* program was used to 'pre-treat' the collapsed fluid element, therefore minimizing the fluid at the wall/fluid interface that would end up creating the tails. Several methods were found for the *shift* transformation, with lateral migration of the central column varying from 10% to 20% of the full channel width (see figure 6(a-ii)), and varying degrees of 'squareness' in the final output. The basic transformation as originally outlined seeks to preserve the shape at the microchannel inlet, and the programs shown demonstrate the best outcome to this effect.

6. Conclusions

We are able to identify a set of fundamental fluid transformations using rationally chosen sequences of pillars. This is made possible by quickly prototyping different pillar sequences in silico, and identifying those sequences that have the desired effect on the fluid shape. The identified transformations have potential applications in optofluidics, shaped fiber and particle fabrication, and mixing. The transformations also provide some intuition on the types of fluid deformations that can be performed using pillars in a

channel.

The framework utilized on this study, although applied here only to pillars positioned in a straight channel, can be used to analyze flow deformation resulting from the concatenation of arbitrary geometries, provided that thefluid is allowed to fully develop in between. Other geometries for consideration include channel expansion regions, curved segments, walls, asymmetric pillars, and channel bifurcations. The analysis can also be expanded to include a range of Reynolds numbers and channel aspect ratios, which were held fixed for this study.

Presently, the effect of diffusion on the fluid is ignored. Large numbers of pillars -and therefore longer channels along with more complex fluid deformations will enhance mass diffusion further downstream, resulting in a blurred departure from uFlow's predicted transformation. Accordingly, mass diffusion will limit the size of structures that can be formed using this method, though diffusion of species across streamlines may be important for many applications. The current framework can be extended to account for diffusion by applying a simple local diffusion model to a fluid parcel as it traverses the channel. Techniques for enabling this analysis in real-time are under investigation.

Although the present study only follows fluid parcels as they traverse the channel, it is possible in principle to apply the same analysis to finite-sized particles suspended in the fluid flow, which may cross streamlines. Although it is more expensive to compute advection maps for finite-sized particles, this computation is performed offline, and does not affect the speed of the analysis.

Building off this initial work, future designers of continuous flow fluidic systems should be able to achieve a desired output behavior without significant rounds of experimental trial and error, paving the way for systems of increased complexity to address biomedical, materials fabrication, and industrial heat and mass transport problems.

7. Acknowledgements

This research is supported in part by the National Science Foundation through XSEDE resources provided by TACC under grant number TG-CTS110007, and supported in part by NSF-1306866, NSF-1307550, and NSF-1149365.

Bibliography

[1] A. P. Sudarsan and V. M. Ugaz, Proceedings of the National Academy of Sciences of the United States, 2006, 103, 7228

[2] X. Mao, J. R.Waldeisen, B. K. Juluri and T. J. Huang, Lab Chip, 2007, 7, 1303–1308.

[3] J. K. Nunes, C.-Y.Wu, H. Amini, K. Owsley, D. Di Carlo and H. A. Stone, Advanced Materials, 2014, n/a–n/a.

[4] A. D. Stroock, S. K. W. Dertinger, A. Ajdari, I. Mezic, H. A. Stone and G. M. Whitesides, Science, 2002, 295, 647–651.

[5] R. H. Liu, M. A. Stremler, K. V. Sharp, M. G. Olsen, J. G. Santiago, R. J. Adrian, H. Aref and D. J. Beebe, Microelectromechanical Systems Journal of, 2002, 9, 190–197.

[6] D. Di Carlo, Lab on a Chip, 2009, 9, 3038–3046.

[7] P. B. Howell, Jr., D. R. Mott, S. Fertig, C. R. Kaplan, J. P. Golden, E. S. Oran and F. S. Ligler, Lab Chip, 2005, 5, 524–530.

[8] D. A. Boyd, A. R. Shields, P. B. Howell and F. S. Ligler, Lab Chip, 2013, 13, 3105–3110.

[9] G. Segr´e and A. Silberberg, Nature, 1961, 189, 209.

[10] H. Amini, E. Sollier, W. M. Weaver and D. Di Carlo, Proceedings of the National Academy of Sciences, 2012, 109, 11593–11598.

[11] H. Amini, E. Sollier, M. Masaeli, Y. Xie, B. Ganapathysubramanian, H. a. Stone and D. Di Carlo, Nature communications, 2013, 4, 1826.

[12] D. Chiu, Analytical and Bioanalytical Chemistry, 2007, 387, 17–20.

[13] A. J. Chung, D. Pulido, J. C. Oka, H. Amini, M. Masaeli and D. Di Carlo, Lab Chip, 2013, 13, 2942–2949.

[14] J. Diaz-Montes, Y. Xie, I. Rodero, J. Zola, B. Ganapathysubramanian and M. Parashar, Computing in Science Engineering, 2014, PP, 1–1.

[15] A. N. Brooks and T. J. Hughes, Computer methods in applied mechanics and engineering, 1982, 32, 199–259.

[16] T. E. Tezduyar, S. Mittal, S. Ray and R. Shih, Computer Methods in Applied Mechanics and Engineering, 1992, 95, 221–242.

[17] R. Jaeger, J. Ren, Y. Xie, S. Sundararajan, M. Olsen and B. Ganapathysubramanian, Applied Physics Letters, 2012, 101, 184102.

In the previous paper, “Micropillar sequence designs for fundamental inertial flow transformations,” we systematically discovered the fundamental operations of the shape of inertial flow in the microchannel and demonstrated our ability to create designed and complex cross-sectional patterns of the flow. In the next paper, we applied this capability to manipulate the spatial distribution of photoinitiator in the liquid polymer precursor and innovated an advanced fabrication method integrated with optics and liquid-handling, called optical Transient Liquid Molding, to synthesize unique 3D shaped microparticles. We demonstrated several microparticles with complicated 3D shapes and integrated functionalities, which were shown in the first time and promising for advanced biomedical studies in the future.

Chapter 3 :

Rapid Software-Based Design and Optical Transient Liquid Molding of Microparticles

Shaped microparticles with complex curvature, holes, and surface or composite heterogeneity enable unique applications in biomaterials (1), self-assembly (2), photonic crystals (3), and encoding (4). Microparticles with shape control and multi-functionality have been engineered to enable advanced technologies, including self-aligned flow cytometry and encoded-microparticle-based multiplexed detection (5, 6). Drug delivery and cell uptake are known to be shape-dependent (7) while assembly of tissue mimetic systems could benefit from 3D interlocking shapes and spatially engineered combinations of constituents (8). Moreover, for scaling up production of therapeutic compounds in cell bioreactors, particles shaped with pores or voids could enhance cell growth, achieving high surface area while protecting cells from high fluid shear stress.

Additive layer-by-layer fabrication processes, such as 3D printing, have allowed for the manufacturing of complex three-dimensional and software-designed objects with holes or voids from a variety of materials (9), but mass-production of microscale objects or features are difficult to achieve. Optical lithography approaches that leverage microfluidic delivery of precursor photopolymer streams, such as stop-flow lithography (10), possess many of the advantages of 3D printing technologies, and have expanded fabrication to microscale objects (i.e. particles) with a relatively high manufacturing rate

that is on an upward trajectory (5, 11). Although recent work has expanded optofluidic lithography approaches, initially limited to extrusions of 2D patterns, to a larger set of 3D shapes (12), the particle shape remains limited compared to 3D printers. Reduction of this limitation can in theory be achieved by shaping the polymer precursor stream prior to extrusion with a 2D pattern.

Structure-induced flow deformation has been used to shape co-flows of UV-crosslinked polymer precursor streams and inert streams to create three-dimensional fibers (13, 14) and millimeter-scale particle shapes (15) following flood or masked UV exposure respectively. The flow deformation can be precisely predicted within a laminar flow regime, Reynolds number, Re < ~ 2000, where Re is the ratio of inertial to viscous effects in the channel (16). We recently demonstrated freeware (called *uFlow*) that allows design of 2D flow shapes with a simple GUI and rapidly performs calculations using the graphics processor unit of a personal computer, allowing real-time prediction of a flow shape. This approach was also used to predict and design shaped fibers (13).

However, a significant challenge for inertial-microfluidics-based lithography is to shrink down the size of fabricated particles to the micrometer scale. Specifically, higher viscosity solutions of the polymer precursors that must be shaped at higher Reynolds number than standard stop-flow lithography lead to pressures that significantly flex the fluidic system leading to long capacitive times and the inability to quickly stop the shaped flow before it transits out of the channel. In our previous work, the strategy to

reach a high Reynolds number necessary to shape a flow and stop flow in a reasonable time was to enlarge the channel size. However, this led to particles that were fabricated at the millimeter scale and required a longer flow development and settling time due to longer timescales for viscous dissipation of fluid momentum. In this article we achieve production of particles an order of magnitude smaller using an approach we call optical Transient Liquid Molding (TLM).

The smaller channel dimensions and unique method of stopping flow in TLM allows us to bridge real-time software design and fabrication, provides advantages in terms faster cycle times for production, and allows production of particles from a wider range of materials. Using this approach, we were able to manufacture hundred-micrometer scale particles with minimum feature sizes of 10~15 micrometers with design of 3D particle shapes *a priori* using *uFlow*. These shapes we generated with high fidelity based on extrusion of an engineered 2D flow cross-section with an orthogonal 2D masked UV light source, qualitatively and quantitatively matching predictions. We also move beyond our previous work to show the compatibility of the system with organic and aqueous photopolymerizable materials, and fabricate microparticles with complex integrated functionality including multi-layered structures, selectively functionalized surfaces, and superparamagnetic nanoparticle-doped microparticles with magnetic anisotropy. The optical Transient Liquid Molding is a universal strategy to rapidly refresh and control high speed flow inside microchannels enabling 3D design of particle shape and layered structures *in silico*, fabricating the design in reality, and finally applying the products in advanced microparticle systems.

Software to rapidly calculate 2D cross-sectional flow shapes has been used to predict flow deformation and related polymer fiber shapes *a priori* (13, 15-17). Importantly, for a sequence of structures, such as ridges (17) and pillars (16, 18), the accumulated flow deformation and final shape of a flow stream can be calculated by sequentially applying the flow deformations from each structure in the channel in series as long as the distance between structures is sufficiently large to prevent fluid dynamic coupling. This approach has been applied to calculate flow shapes by pre-computing the set of individual flow deformations (2D advection maps) accompanying a finite set of structures and positions (16, 19), and instead of solving the full Navier-Stokes equations for a new sequence of structures, applying the 2D advection maps for each structure in this new sequence.

We use software developed in-house to assemble sequences of advection maps interactively, allowing rapid design of the final fluid cross-section by utilizing the massively parallel computational capability of modern graphical processors. First, Navier-Stokes equations are solved offline in a finite element solver. A GPU-based particle tracer is used to convert the flow fields into 2D advection maps in a reasonable time (less than one second per map). To increase efficiency processing units on the graphics card can be assigned to perform particle tracing in parallel. The mapping for each element in the domain can be finished simultaneously, decreasing the time consumption of mapping by at least three orders of magnitude. 12,895 advection maps

are assembled into a library, each map corresponding to a different structure. Principle component analysis (PCA) is used to compress the library and produce new structures by interpolation. Advection maps are reconstructed and assembled on modern GPUs in less than 10ms, allowing interactive use. A simple diffusion model is applied: after each structure, a fluid particle spreads into neighboring streams according to a Gaussian distribution with $\sigma=(t^*/Pe)^{1/2}$, where t^* is a time each fluid parcel takes to pass through a structure and Pe is the Peclet number (defined and discussed later with the fabrication system). The final particle shape is rendered by raymarching. A video shows real-time operation of the software, from user input to final 3D shape (Supporting Information Movie S1). The software is also freely available on our lab website: http://biomicrofluidics.com/software.php. In parallel, we are also working on solving the inverse problem to rapidly compute a sequence of structures that will yield a desired 2D flow shape[18], which would allow generation of shapes based on a user-defined CAD drawing.

The fabrication system consists of two sub-systems: an inertial flow deformation system with a microchannel programmed with microstructures to yield a desired cross-sectional flow shape and a computer-controlled pressure and UV exposure setup, shown in **Figure 1(a)**. Both sub-systems are automated with a custom LABVIEW program. In the first sub-system a polymer precursor stream (consisting of monomer and photoinitator) is sheathed by flows of monomer without photoinitiator to achieve a combined channel Reynolds number (Re) of 5~40 through the microchannel with embedded microstructures. The Re is defined as $\rho U_0 H_h/\mu$, where $H_h=4A/p$, A is the cross sectional

area of the channel, p is the perimeter, U_0 is the average flow velocity, ρ and μ are density and viscosity of liquid respectively. At this *Re* the polymer precursor stream is sculpted by the microstructures in the microchannel due to the combination of net flow deformations around the structures (16). 10 mm downstream of the final microstructure a fully-shaped stream is available in an unobstructed microchannel for UV illumination by the second sub-system. In the second sub-system, which differs significantly from our previous work, the sculpted flow is pressurized upstream and downstream to rapidly stop and form the transient liquid-liquid 3D interface. This interface will blur with time due to diffusion, however, rapid UV exposure through a de-magnified mask after the flow stream is stopped minimizes blurring in the generated particles. To fabricate particles with the same shape continuously, the deformation of the flow stream, pressurization, and UV exposure are repeated in series, wherein individual timing is controlled using our automated program.

Four steps were run in series to finish one process cycle and replicate one 3D particle. *Step 1:* The precursor and monomer streams were pumped into the microchannel with designed micropillars using a computer-controlled syringe pump (Harvard Apparatus, PHD 2000) at a set *Re* to form the precursor stream with a pre-designed cross-section once the flow was fully developed. During the initial step 1 of a continuous cycle, we spent 5 minutes to completely pressurize the microchannel and reach a fully-developed flow. *Step 2:* The downstream valve is switched closed and the syringe pump is turned off, pressurizing downstream of the channel to stop the flow without disturbing the shape of the flow stream. We allowed for one second for flow to stop because

elongated particles were observed when the time between step 2 and 3 was less than one second. *Step 3:* The shutter is opened allowing UV illumination through an optical mask demagnified by a 10X objective onto the target location of the stream for 0.5 to 1.5 seconds. The UV power is set to be 8.6~17.7 mW/cm^2, measured by a power meter (PM206, ThorLABS). The intersection of the precursor stream and optically-masked shape forms the 3D photopolymerized microparticle inside the microchannel. *Step 4:* The polymerized particle is washed downstream and a new liquid mold is reformed 5 to 10 seconds after the downstream valve is switched open and the syringe pump is turned on again. These four steps are then automatically repeated to fabricate particles at a rate of ~720 particles/hour (see Supporting Information Movie S2). To create larger numbers of particles without user intervention, we automated the control of a valve (ASCO Scientific ®, 2-Way Pinch Valve, Catalog Number: SCH284A003), connected to the outlet of the microchannel with a 10 cm tygon tubing to stop flow, and control of a shutter (Lambda SC, Smart ShutterTM control system) for UV illumination (Excelitas Technologies, OmniCure ® S2000 UV Curing System) of the stationary liquid mold. The outlet of the valve is connected to a particle collector reservoir which includes a filter to accumulate particles. The time plots of the system parameters over the four steps are shown in Figure 1(b). The times between step 2 and 3, step 4, and step 5 are referred to as the diffusion time, exposure time, and flow recycling time respectively. The longest step is in re-establishing the steady-state flow shape defining the liquid mold, after stopping flow. Because of the pressure built up during flow stoppage and the maximum pressure rating of our pinch valve, the working range for precursor solution viscosity when Re equals to 10 was <15 mPa·s. On the other hand, when the capacative

timescale is not dominant, the flow stoppage time is dominated by the timescale of viscous dissipation, H_h^2/v, where v is the kinematic viscosity. Unlike for previous stop flow lithography systems, for these inertial flows, less viscous fluids, such as water (~ 1 mPa·s), required a longer flow stoppage time and were less ideal.

The shape of molded particles depends on an energy threshold of photopolymerization, the spatial distribution of photoinitiator, andthe optical system. There are two diffusive parameters influencing the local concentration of photoinitiator in the two sub-systems respectively. In the first sub-system, the molecules of photoinitiator diffuse in the direction perpendicular to the flow direction during flow. The relative amount of convection of the photoinitiator in the flow downstream versus diffusion cross-stream is described by the Peclet number, Pe= U_0W/D, where D is the diffusion coefficient of the photoinitiator (D= ~ 10^{-6} cm^2 s^{-1}) and W is the width of the microchannel. In *uFlow* we use Pe along with estimated relative time of flight information for each fluid parcel to predict the diffusive blurring of the shape. After the flow is stopped, in the second sub-system, the molecules of photoinitiator diffuse uniformly in all directions. The more quickly the flow is stopped and UV exposure is applied, the more faithfully the created particle will replicate the predicted particle shape. On the other hand, the time period to stop the flow and UV illumination delay time can also be used to tune particle shape. Here, we mainly allowed for a diffusion time of ~1s (diffusive distance after the flow stops of 1~10μm) to minimize the error caused by diffusion (calculated by *uFlow*). We also vary this parameter and discuss how the dimensions of particles evolve as a function of diffusion time. In *uFlow*, we generate a particle shape as a function of a

polymerization threshold, or minimum energy for polymerization which is the function of local concentration of photoinitiator and UV energy. Precise prediction of dimensions can be achieved by calibrating the threshold in comparison to experimental measurements. We investigated the effect of fabrication parameters, related to control of the fluid, diffusion, and photopolymerization, on the dimensions of microparticles. We measured two dimensions of C/triangle microparticles, the thickness in the middle of the "C" which should depend on the inertial flow sculpting and diffusion, and the height of the triangle which should depend on photopolymerization effects, while four parameters: flow recycling time, diffusion time, exposure time, and Reynolds number, were varied (Figure SI2). The first dimension reached a steady state when the flow recycling time was over five seconds indicating the flow became fully-developed in this time period. "C" width increased monotonically with increasing diffusion time, but remained relatively uniform for times less than 2 seconds indicating that UV illumination was fast enough to neglect significant diffusion following flow stoppage. UV exposure yielded a less continuous change in dimension, jumping from zero to a finite value when the exposure time was over 300 ms and then increasing monotonically, indicating an energy threshold for photopolymerization. The thickness of the "C" is sensitive to flow rate or Reynolds number and became monotonically smaller with increasing Re. Higher Re introduces stronger flow deformations, stretching out the C shape as predicted in *uFlow* (Figure SI2(a) bottom). On the other hand, we observed that the triangle height dimension mainly varied with the exposure time, because this shape depends almost entirely on the shape of the photomask. Because the photomask is focused onto the microchannel plane and the depth of focus (~50 μm) was comparable or less than the

liquid mold dimensions, we could expect variation in UV light intensity and some variation in the particle width dimensions as a function of height. We found the deviation of particle width was less than 10 degrees based on the images of fabricated particles. In *uFlow*, we assumed the tilting angle of UV light is negligible and UV light is considered to be perpendicular to the flow direction leading to some discrepancy. In addition to optics, the liquid-liquid interface also can play a role in the modulation of particle shape from predictions. In fabricating (poly(ethylene glycol) diacrylate, PEGDA, MW~575) microparticles, the amount of photoinitiator in the precursor was negligibly small and all other aspects of the materials were identical leading to high agreement between fabrication and prediction, excluding any interfacial modeling. For NOA89 mircoparticles, the viscosity discrepancy between NOA89 and TEGDM sheathing solutions lead to a larger error in the lateral dimensions while the interfacial tension was still negligible for these miscible solutions. In sum, the dimensions related to inertial flow deformation and generation of the liquid mold depend on all controlled parameters while the dimension related to mask design is only governed by optical parameters.

Eleven types of microparticles were fabricated and compared with *uFlow* predictions. C/triangle microparticles were fabricated using aqueous photo-crosslinkable polymer PEGDA with Re~10, flow recycling time=5s, and exposure time=1s. Diamond/ellipsoid and nine other types of microparticles were made using organic solvent based UV optical adhesive (NOA89, Norland), pumped at Re~8 with flow recycling time=5s, and exposure time=500ms. We define systematic error in particle shape as the difference between average dimensions of manufactured particles and *uFlow* predictions and

random error as the difference between average and individual dimensions of a particle type in an experiment.

Microparticles fabricated using hydrogels (PEGDA) and UV optical adhesive (NOA89) possessed 3D shapes in qualitative and quantitative agreement with *uFlow* predictions (Figure 2 and Figure SI1). Each calculation and visual display of a new 3D particle shape occurred in near real-time in software allowing interactive exploration and design of particles. Once settling on a design, micropillar mask designs and flow stream ratios provided by *uFlow* were used to fabricate and operate the microfluidic liquid molding devices. Photopolymerized PEGDA particles showed good qualitative agreement with *uFlow* predictions from multiple angles. Four images compare the *uFlow* prediction (left column) with the fabricated particle shape (right column) from different viewing angles Figure 2(a). In this case the predicted liquid mold consisted of a curved void space and a particle with a qualitatively matching curved surface was replicated. To quantify the similarity between the predicted and fabricated particles the distance between two points at the tip of the “C” of these microparticles were measured and agreed with predicted values with < 1% systematic error on average. We also confirmed the repeatability of the fabrication system achieving <3% random error on average. Diamond/ellipsoid microparticles fabricated using organic solvent based UV optical adhesive also agreed with predictions. Two orientations were shown in Figure 2(b) for each particle type, consisting of the ellipse major axis in a horizontal or vertical position. In the horizontal one, there was a systematic error of ~19% in distance across the diamond, in which fabricated particles were always observed to have expanded

dimensions. We fabricated nine additional microparticle types with various combinations of liquid molds and UV patterns demonstrating the robustness, qualitative accuracy, and repeatability of fabrication (Figure SI1).

We also could predict and fabricate particles with multiple integrated functionalities by molding multiple co-flows of separate composition. Using separately dyed precursor streams we show that the distribution of green and red fluorescence can be molded into the particle cross-section in agreement with the structure designed in software (Figure 3(a)). We also demonstrated the ability to selectively functionalize a surface of a particle (Figure 3(b)). We created particles with biotinylated internal surfaces which displayed selective binding to fluorescent streptavidin in these regions. Without incorporation of biotinylated PEG precursor into a precursor stream there was relatively low fluorescence intensity across the entire particle (Figure SI3). Besides showing the ability to selectively functionalize a pre-defined region these results indicate that the biotin could retain reactivity after UV exposure.

Using optical TLM of magnetic doped precursors we were able to fabricate magnetically anisotropic particles that could be oriented in 3D in an external magnetic field. We designed C/circle magnetic microparticles using *uFlow* (Figure 4(a)). The high transparency of the fabricated magnetic microparticles without accumulation of clusters of magnetic nanoparticles indicated a homogenous distribution was achieved and magnetic properties could be considered uniform throughout the particle shape.

However, because of the asymmetry in particle shape these particles were expected to respond and orient to a preferred axis in response to an external magnetic field. We numerically and experimentally explored aligning and orienting these particles to arrays of magnetic gradient (and force) amplifying micromagnets (20). We modeled a particle with the target orientation placed in between two micromagnetic elements using finite element method with COMSOL Multiphysics and following calculation of force integraed magnetic torque per unit area induced by the Maxwell stress tensor across the esntire surface of the particle to arrive at the net torque applied on the particle with each orientation. Simulation results show that the orientation of the magnetic microparticle in the presence of a nearby micromagnet is stable at 90 degrees (and -90 degrees due to symmetry), where the opening of the particle faces to right (or left) (Figure 4(c)). We randomly spread the magnetic microparticles on the substrate (Figure SI4) and then applied an external magnetic field to attract a microparticle to the bottom edge of each magnetic element (see Supporting Information Movie S3). The attracted microparticles were observed to be orient their open face to the right, agreeing with simulation. The attracted particles could then be moved along the edges of the magnetic elements with a corresponding change in the external magnetic field direction in the 2D plane. Moreover, because of the magnetic anisotropy of the 3D shaped particle, shifting the magnetic field direction out of the 2D plane by rolling the external permanent magnet guided the attracted microparticles to rotate out of plane in 3D, presenting an open face (Figure 4(d), Figure SI4, and see Supporting Information Movie S4).

We have demonstrated that complex 3D shaped microparticles with 100-micrometer scale dimensions can be fabricated matching interactively pre-computed software-based designs, including multi-layered particles, selectively functionalized surfaces, and two separate UV-polymerizable base materials. In order to achieve fabrication at the micrometer scale, optical TLM reduces the long capactive and viscious dissipation of momentum timescales which leads to pressure, velocity, and diffusion fluctuations as flow stops, and significantly destroys the shape of flow streams. The decreased channel dimensions that are enabled with this approach also allows enlarging the space between micropillars, decoupling the fluid dynamic interaction between each pillar and enabling the use of *uFlow*-based real-time designs.

Although we are able to faithfully replicate predicted particle shapes with a low degree of error, for some applications requiring improved precision the current technique may require further optimization. Deviations of the particle shape from predictions is determined by the combinatorial effect of the optical exposure system, generation of the 3D liquid-liquid interface, and the dimensional tolerances in the fabricated microchannel. Within the masked shape, the dimensions of the particle is mostly defined by the transient liquid mold while the edges of the particles where the mask cuts into the transient liquid mold are the coupled result of the molding process as well as depth of focus (Rayleigh range) affecting the UV light intensity distribution. Moreover, the dimensional and parameter error of the fabrication system includes dimensional error of the flow shaping microchannel, error in setting the proscribed Re and Pe, an initial curved liquid-liquid interface when the precursor stream is initially sheathed (21),

calculation error in the flow rate for each stream, and limits in control of diffusion and exposure time. We also found that physical contact of the edges of the liquid mold and walls of the microchannel led to reduced accuracy in flow shapes, potentially due to oxygen inhibition. Additionally, there are currently limitations in the speed of 3D particle generation, mainly due to the flow recycling time of 5 seconds required to reach the steady-state liquid mold. Technically, the throughput of optical TLM can be improved using parallelization of the optical mask or the microfluidic channels. Further optimization of the fabrication process especially for flow recycling to reduce fluidic capacitance and inductance should also enhance production rate.

In the short term, the introduction of 3D shapes with holes and voids is enabling for advanced biomaterials (22) as well as materials with unique anisotropic mechanical, chemical, magnetic or optical properties. 3D microparticles with shape-dependent mechanical properties can be potentially applied as biosensors for the study of single cell mechanics while porous particles with selective adhesive regions within pores could serve as high surface area carriers for adherent cells in bioreactors while protecting the adhered cells from shear stresses accompanying transport of the cell carriers. Microparticles in the hundred micrometer size range can self-assemble by applying external forces, e.g. capillary force, and designing interlocking shapes on the particles (23). For the application of photonic crystals, instead of making small particles the periodic structure or the complex anisotropy of composition with or below 10μm scale can be sculpted on or within particles , generating unique photonic properties[24]. For drug delivery and cell uptake, smaller particles can be produced using a few

approaches in the future: by locally polymerizing the precursor stream, sheathing and engineering the precursor stream sequentially to reduce its size, or shrinking channel dimensions, which also has the benefit of enhancing viscous dissipation of momentum, although increasing the pressure to drive the flow. In addition, the anisotropic magnetic particles produced can be used for magnetically controlled inks (25), control of micro optic components (26), manipulation of microreactors or microcarriers with cells to be viewable, active sorting of microcarriers, and micro-actuators with soft structures (27). Combined with computationally efficient solutions to the inverse problem (28) for a full 3D shape, and re-configurable structures within a microchannel (29), the presented techniques lay the ground-work for rapid reconfigurable production of a large set of 3D micro- to centimeter-scale objects using standard CAD software.

Experimental Section

Fabrication of microchannels and microfluidic connections: We fabricated microchannels (300μm by 1200μm) with micropillar sequences predicted to achieve a desired cross-sectional shape using soft lithography. The molds were made of two layers of photoresist (SU-8 2100, MicroChem Corp.) patterned by photolithography on a wafer. Precursor and curing agent of Polydimethylsiloxane (PDMS, Sylgard 184, Dow Corning) were mixed at a 10:1 v/v ratio, poured onto the mold, left in a vacuum, and then cured in a 65 ˚C oven. The replicated PDMS chip, punched at inlets and outlet with 1/32” holes, and a slide glass were treated with air plasma (Plasma Cleaner, Harrick Plasma) for 30 seconds and then bound together to enclose the microchannels. The inlets of the chip were connected to syringe pumps using PEEK tubing (0.08” x0.124”,

Cat. Number: 1544, IDEX Health & Science). We inserted a segment of Tygon tubing (Cat. Number: SC0016, IDEX Health & Science) into the pinched valve and connected one side to the outlet of the chip and the other to a separate particle-collecting filter.

Polymer precursor material: We fabricated microparticles with complex 3D shape, multi-layered structures, selective biotinylated surfaces, and magnetic properties, using rigid cross-linked polymer and hydrogel materials. For rigid thiolene polymer particles, we used the UV optical adhesive (NOA89, Norland) mixed with 5% wt of 2,2-Dimethoxy-2-phenylacetophenone (DMPA, 196118, Sigma-Aldrich) for the liquid mold and the sheath streams were triethylene glycol dimethacrylate (TEGDM, 261548, Sigma-Aldrich). For hydrogel particles both precursor and side streams were diluted poly(ethylene glycol) diacrylate (PEGDA, MW~575, 437441, Sigma-Aldrich) with and without 0.67% v/v photoinitiator (2-hydroxy-2-methylpropiophenone, Darocur 1173, 405655, Sigma-Aldrich)). PEGDA was diluted with Dulbecco's phosphate buffered saline (DPBS, SH30028 Thermo ScientificTM HyCloneTM) by a ratio of 2 over 3. Viscosity of the four liquids was measured using a rheometer (Physica MCR 301, Anton Paar®), shown in Table SI1. The Young's modulus of particles made of diluted PEGDA and NOA89 were estimated to be 1.58 and 1.84 GPa respectively by measuring the bulk cured cylinders of two materials using an advanced materials testing system (Instron 5564). Fifty to one hundred microparticles were produced with each 3D shape and images were taken using bright field microscopy at the position of the downstream collector where particles accumulate following wash out of remaining monomer.

Fabrication of particles consisting of multiple materials: To demonstrate production of microparticles composed of multiple components, we co-flowed precursor stream

(NOA89, thiolene polymer), a mixture of precursor and Rhodamine-B, and a mixture of precursor and green fluorescent beads (0.9μm in diameter) as inputs prior to inertial flow shaping. For microparticles with selective biotinylated surfaces, we used the aqueous precursor (PEGDA) with and without Biotin-PEG-Acrylate to make a co-flow and polymerized the shaped stream. We synthesized Biotin-PEG-Acrylate using Biotin-Hydrazide (1.25mg mL^{-1}, B7639, Sigma-Aldrich) and Acrylate-PEG-NHS (5mg mL^{-1}, MW~5000, Laysan Bio, Inc.) in DPBS. After manufacture, fluorescently-labeled streptavidin was incubated for 1 hr with particles with and without biotin regions. These two kinds of particles were imaged using both bright field and fluorescence microscopy to visualize the layered structure and selective binding to biotinylated surfaces of the particles.

Micromagnetic particles and manipulation: To create particles with magnetic properties, the organic NOA precursor was mixed with superparamagnetic iron oxide nanoparticles (ION, 20 nm in average diameter) to fabricate 3D shaped superparamagnetic microparticles. We isolated IONs from an ION suspension in toluene (700304, Sigma-Aldrich) using a permanent magnet and then resuspended IONs in NOA with DMPA to reach a concentration of ~5mg/mL for fabrication. After fabrication, the microparticles were incubated in 1% w/v Pluronic solution (Pluronic® F-127, P2443, Sigma-Aldrich) for 1 hr to avoid aggregation. We localized shaped magnetic particles to substrates with embedded micromagnet arrays by magnetizing the micromagnets in controlled directions using an external ~0.3 T permanent magnet. The micromagnets in the substrate amplify the magnetic field gradient locally, enhancing magnetic force. PDMS substrates with arrays of micromagnetic elements (500μm by 500μm) were fabricated

as previously described[30]. The 3D shaped magnetic microparticles were transferred from the collector to a well with a thin glass slide bottom with thickness of 0.085-0.12mm (63751, No. 0, Gold Seal®), which has been treated with air plasma for 30 seconds. The substrate with micromagnetic elements was temporarily attached to the bottom of the glass slide and a permanent magnet was then placed on the side of the well to magnetize the magnetic array and attract microparticles to the array locations. The orientation and positions of the magnetic microparticles were recorded using bright field microscopy for different orientations and positions of the permanent magnet. We calculated the torque applied on a particle using electromagnetics finite element modeling in COMSOL Multiphysics where we assumed uniform magnetic field in the whole domain and permeability across the particles.

Supporting Information

Supporting Information is available from the Wiley Online Library or from the author.

Acknowledgements

The authors thank Drs. Baskar Ganapathysubramanian and Dan Stoecklein from Iowa State for the pre-computed advection maps and technical discussion, Dr. Aram J. Chung at RPI for his technical support, Dr. Westbrook Weaver at UCLA for his suggestions of chemical preparation, Dr. Peter Tseng at Tufts Univ. for his help on PDMS substrate with magnetic elements, Dr. Jere Harrison at UCLA for the magnetic

field measurement, Mr. Jaekyung Koh at UCLA for the Young's modulus measurement and Mr. Elias Sideris at UCLA for the viscosity measurements. This work is partially supported by a grant from the National Science Foundation (NSF 1307550).

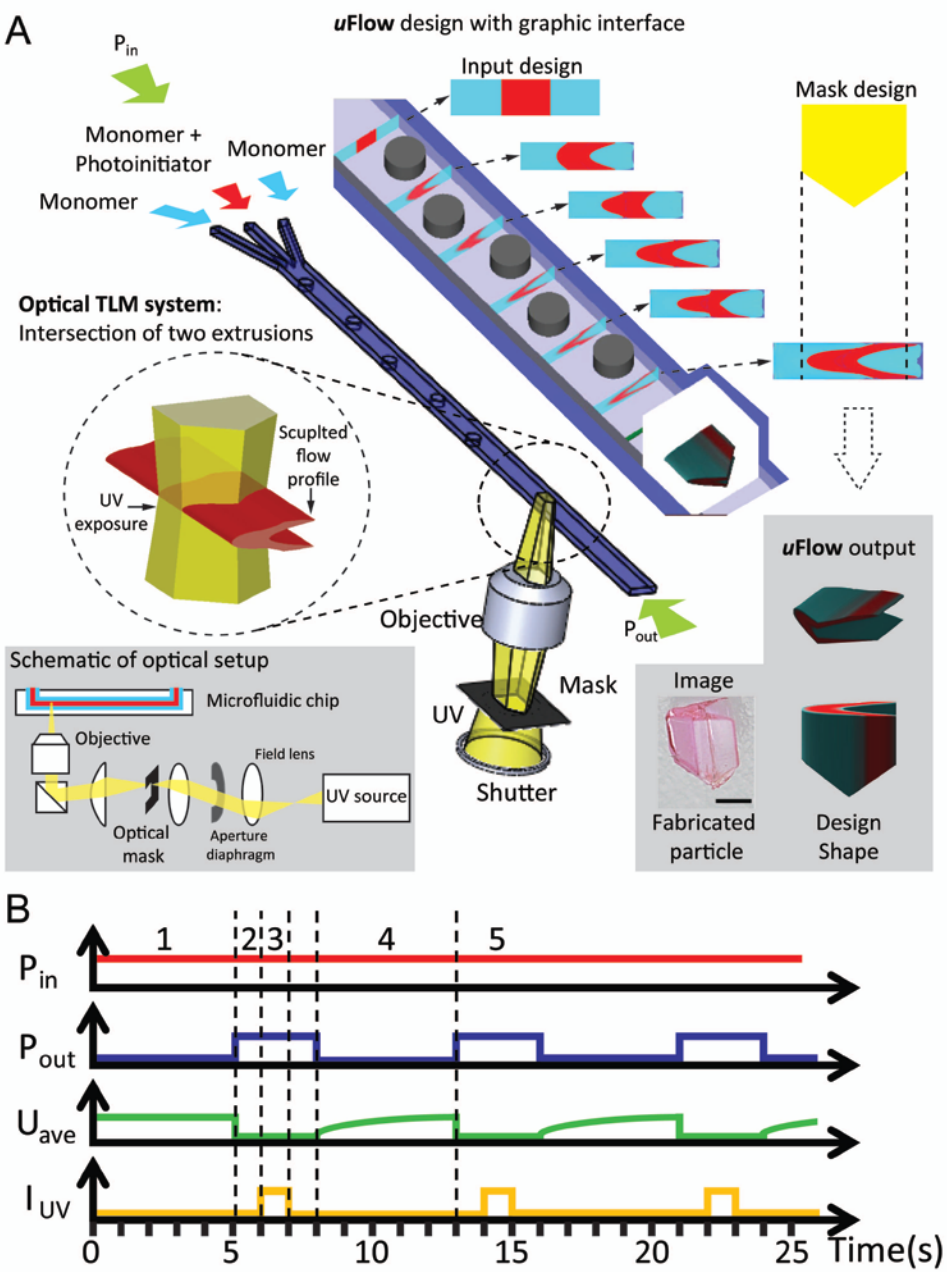

Figure 1. Optical transient liquid molding system and *uFlow* design interface for 3D shaped particles. (a) Integration of two sub-systems: inertial flow engineering and masked optical exposure is shown. The fabricated microparticle is formed by the intersection of two extrusions of the liquid mold and masked UV light, shown in the bottom left circular inset. The scale bar represents 300μm. The insets in the right column represent software design using *uFlow*. In *uFlow*, the cross-sectional shape of a liquid mold is created by arranging micropillars in a sequence within a microchannel. The 3D illustration of the shaped particle is automatically generated downstream. (b) Time plots of four system parameters, inlet pressure P_{in}, outlet pressure P_{out}, average

flow velocity U_{ave}, and UV intensity I_{UV}, for the cycled 4 steps required for 3D shaped particle fabrication. Step 5 represents another cycle of 4 steps in the plot.

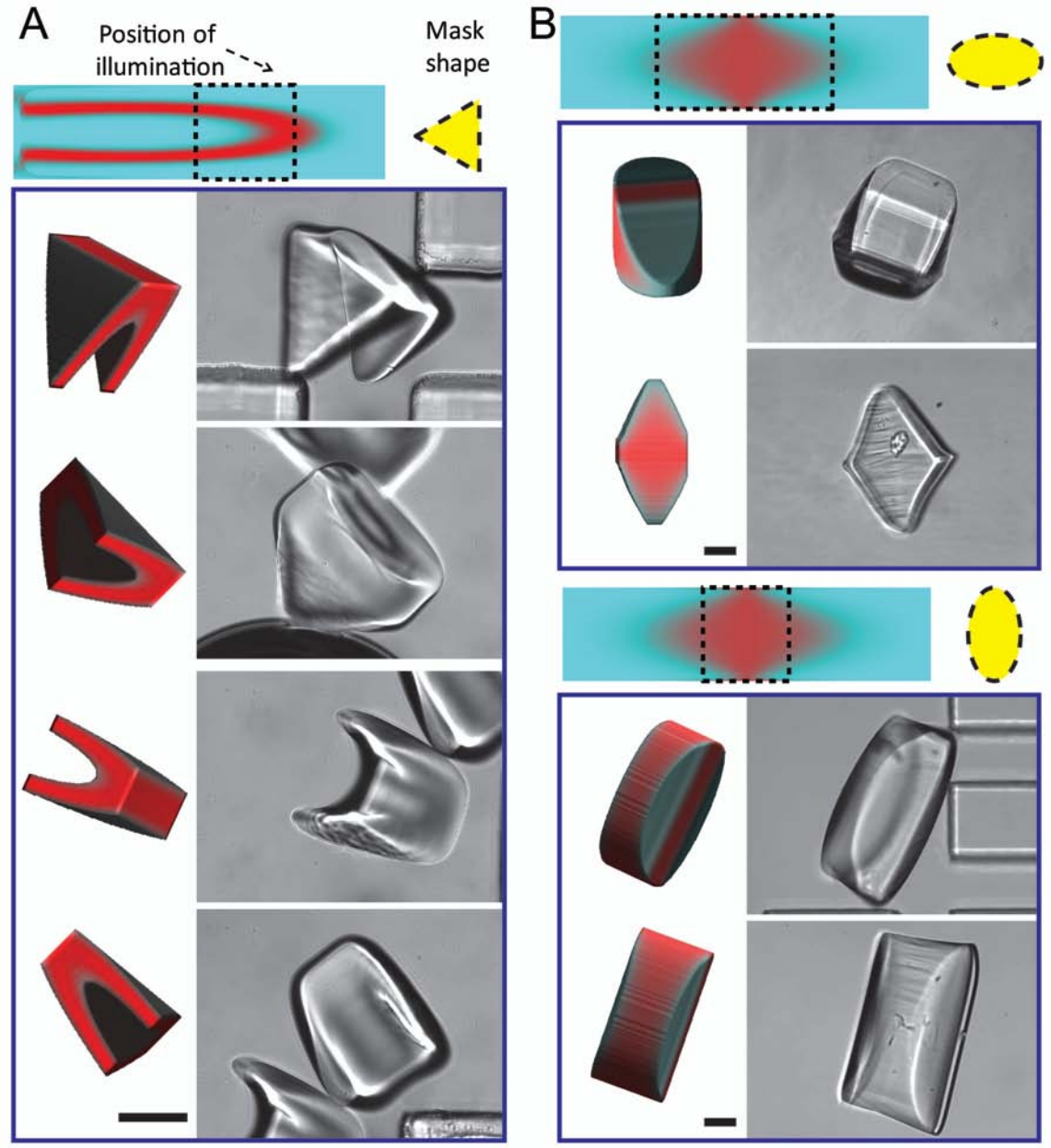

Figure 2. *uFlow* design predictions and fabricated microparticles (a) C/Triangle microparticles made of PEGDA viewed from multiple angles and (b) diamond/ellipsoid particles composed of thiolene polymer. The predicted cross-sectional shape of the precursor stream is marked in red, while the dashed rectangle represents the location of UV exposure for each design. The mask design is shown as a dashed contour and yellow fill. For each predicted 3D shape the corresponding experimental shape was generated and is shown on the right hand side. All scale bars represent 100μm.

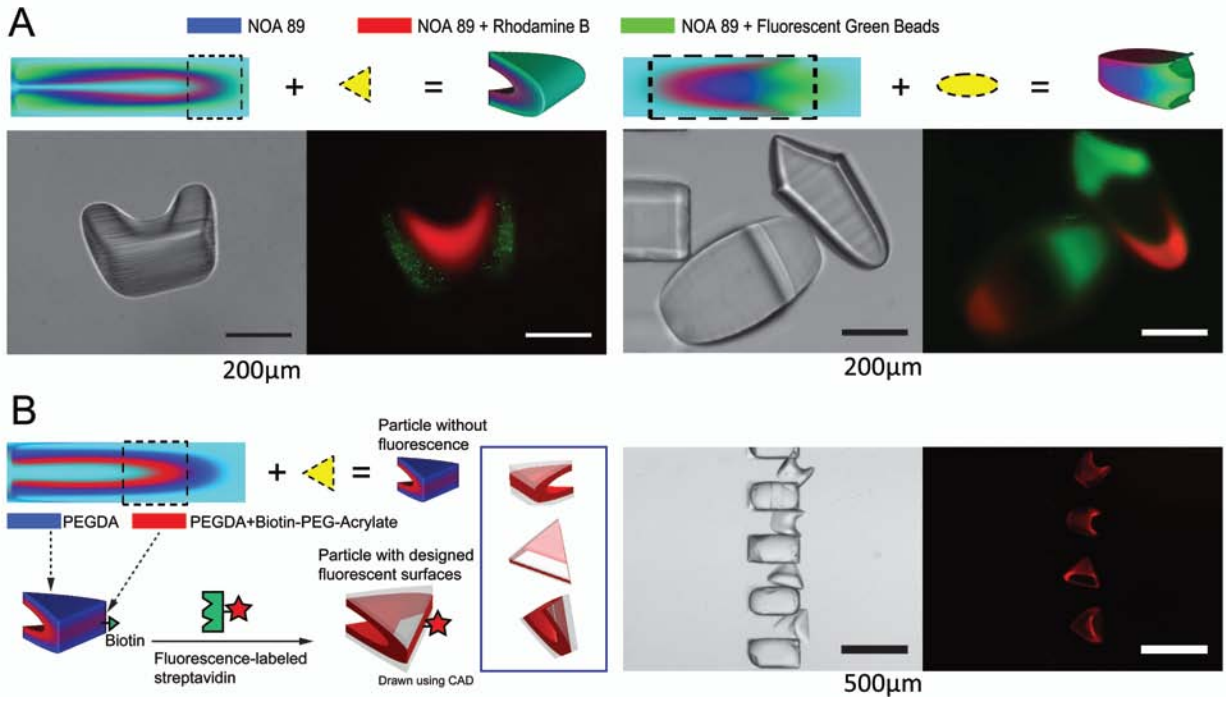

Figure 3. Design and images of 3D shaped microparticles with multi-layered structures and biotinylated surfaces. (a) The left set of images shows the C/triangle microparticle with a layered structure in brightfield and fluorescence. Fish/ellipsoid microparticles with an encapsulated structure are shown on the right. Green fluorescence corresponds to green fluorescent beads and red fluorescence corresponds to Rhodamine-B. (b) C/triangle microparticles with biotinylated inner surfaces and middle layers were designed and tested for biotin functionality by binding with fluorescent streptavidin. The fluorescence distribution of microparticles predicted by *uFlow* (middle) agree with the experimental images on the right hand side.

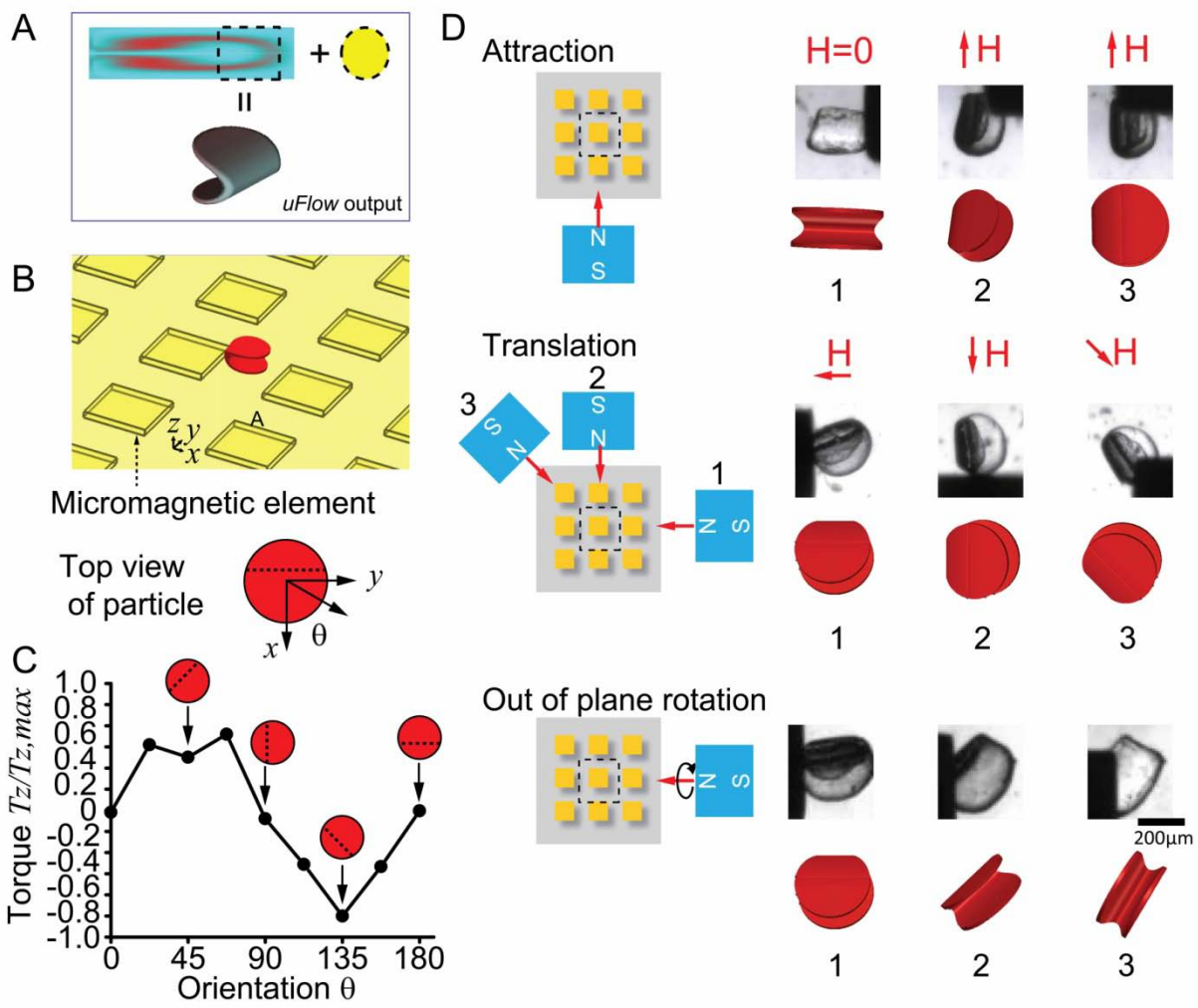

Figure 4. Controlling the position and orientation of anisotropic magnetic microparticles. (a) A magnetic microparticle, shaped by the intersection of extrusions of a C and circle is shown. (b) Simulation domain of magnetic microparticles on a substrate with an array of micromagnetic elements. (c) Simulated torque applied on the microparticle versus the orientation identifies an equilibrium rotation at 90 degree. (d) Sequential images for three types of motions of magnetic microparticles with a shifting external magnetic field: attraction, translation, and out of plane rotation. The left schematic represents the position of the permanent magnet in relation to the substrate. Three sequential images for each type show the initial, transient, and final position and orientation of the microparticle.

Supporting Information

Rapid Software-Based Design and Optical Transient Liquid Molding of Microparticles

Chueh-Yu Wu, Keegan Owsley and Dino Di Carlo[*]

Table S1. Viscosity of polymer precursor materials.

Material	Viscosity (mPa·s)
PEGDA (MW~575) diluted by DPBS with a ratio of 2 over 3	6.8
Diluted PEGDA with 0.67% v/v Darocur 1173	6.6
NOA 89 with 5% w.t. DMPA	15.8
TEGDM	8.5

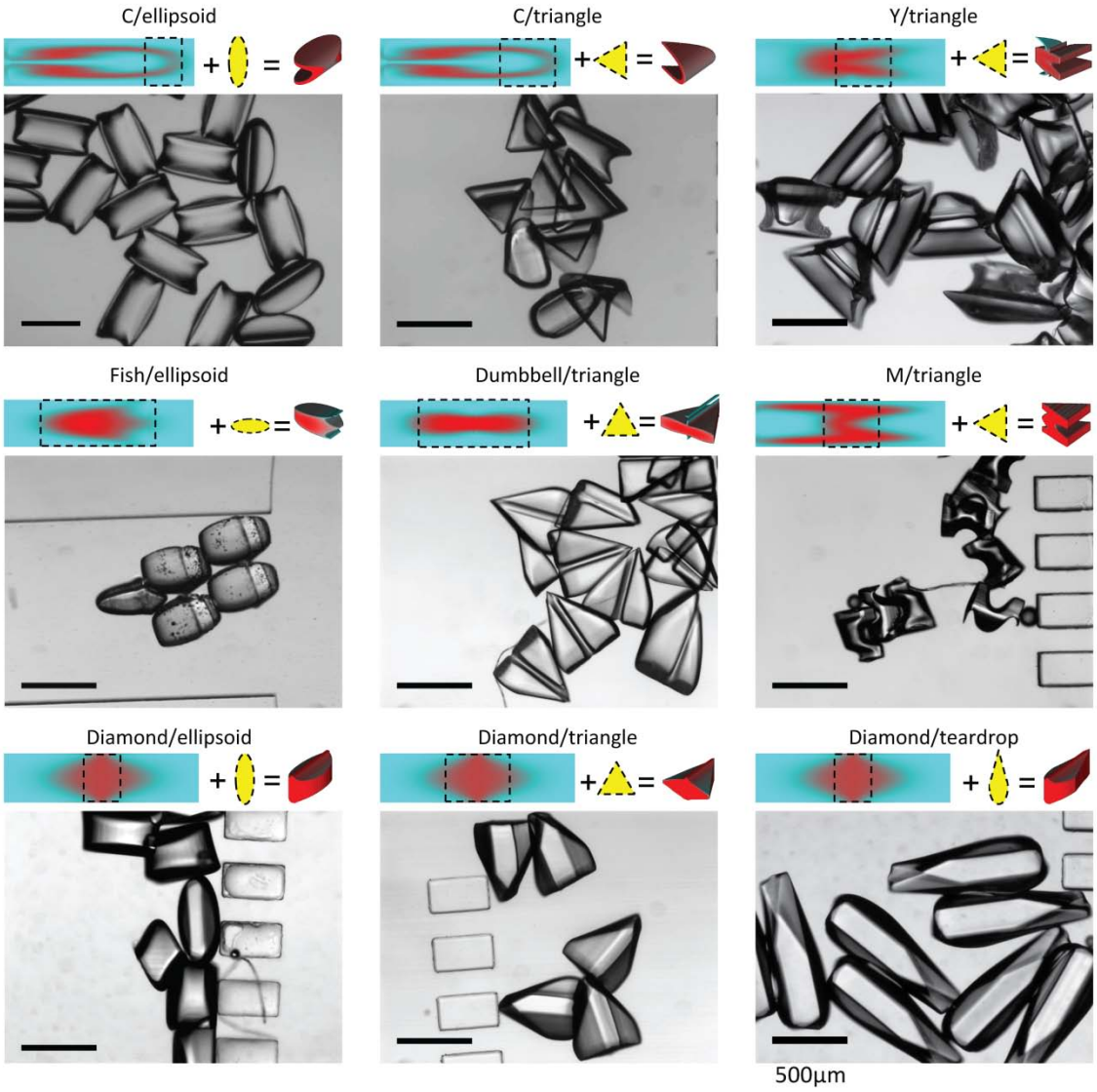

Figure S1. Various 3D shaped microparticles predicted using *uFlow* and fabricated using thiolene polymer. The 3D shapes were selected for the purpose of intuitive illustration of the intersection of two extrusions. We used six types of designs of the cross-sectional liquid mold shape: C, Y, fish, dumbbell, M, and diamond shape. Three types of optical masks were also used: triangle, ellipsoid, and teardrop asymmetric shape (teardrop). The comparison between particle images (bottom) and computational predictions (top) shows qualitative agreement in 3D and both directions of extrusion. The fabrication results of shapes with liquid molds far from microchannel walls, for example, C, fish, dumbbell, and diamond shape, achieve higher quality production of the pattern. Asymmetry of the Y shape and slight loss of top or bottom regions of the M shape were observed likely due to the physical contact between microparticles and walls.

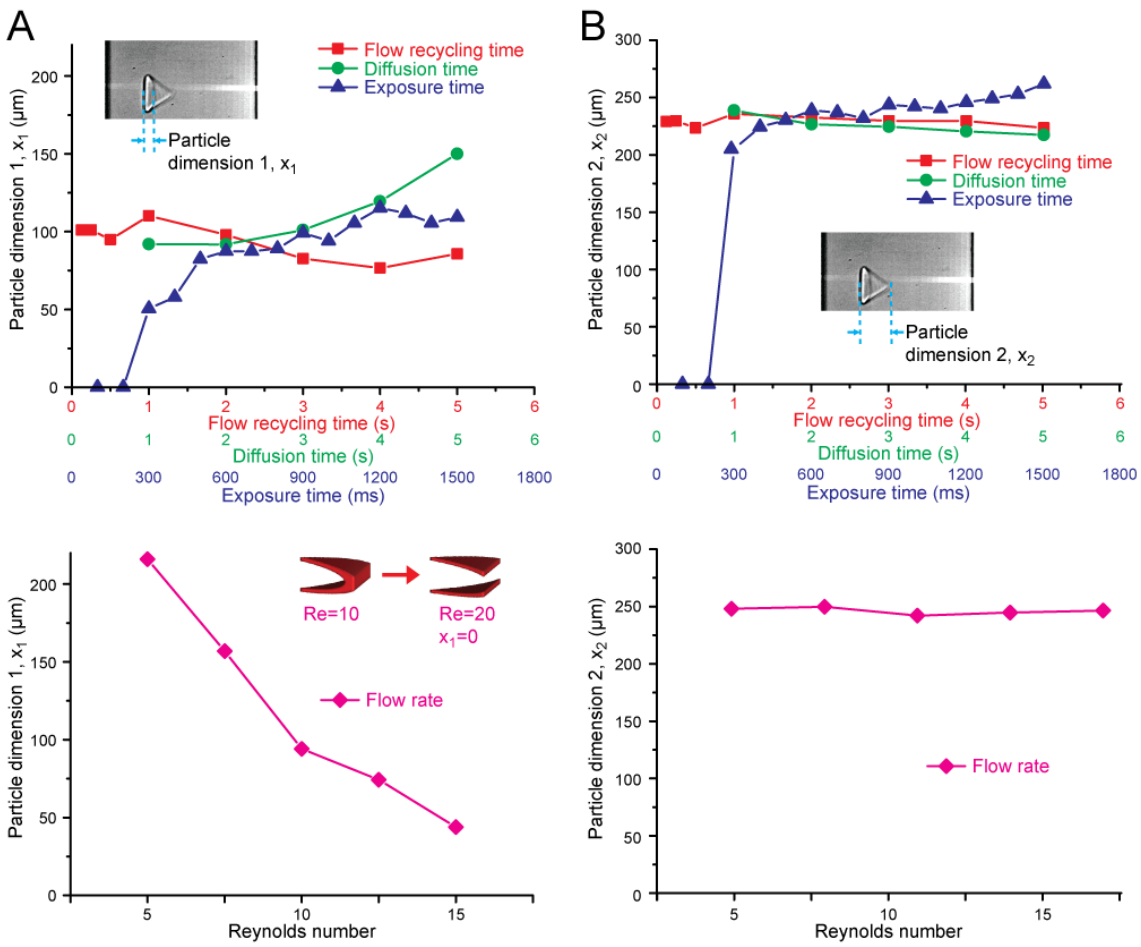

Figure S2. Characteristic dimensions of fabricated C/triangle microparticles as a function of system parameters. The thickness of the middle of the C (particle dimension 1) and the height of triangle from base to point (particle dimension 2) are analyzed. (a) Dimension 1 reached saturation when the flow recycling time was over 4~5s and diffusion time was decreased below 1~2s. Over 300ms, a larger exposure time amplified the size of dimension 1. In the bottom figure, stronger secondary flow caused by higher flow rate yielded a thinner dimension, experimentally. The inset shows that dimension 1 becomes smaller when Re is increased (zero when Re=20), predicted by *uFlow*. (b) Dimension 2 only increases with exposure time, while it remains constant with changes of the other three parameters.

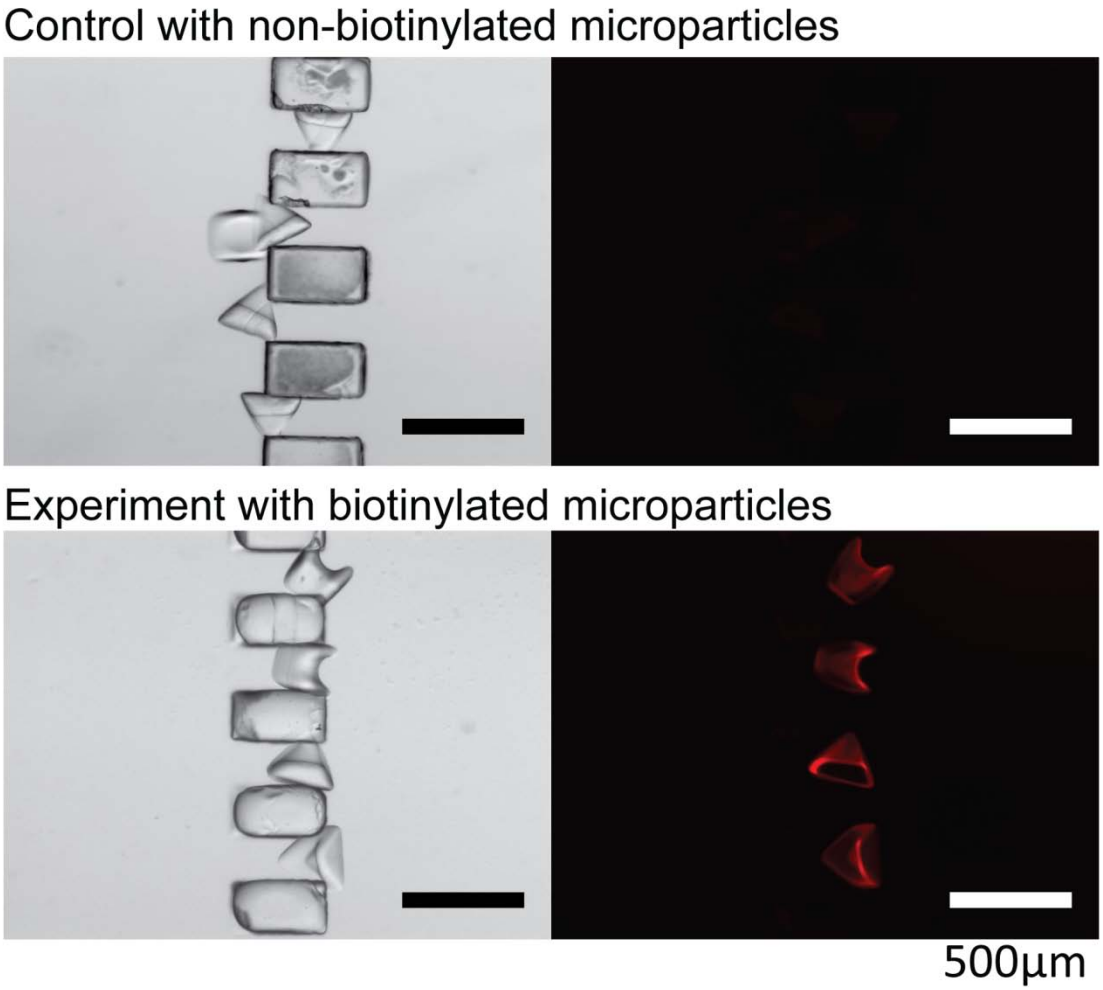

Figure S3. Control and experimental group for biotinylated microparticles. In the top right figure, control particles show there is no fluorescently-labeled streptavidin attached on the surface of particles without biotinylated precursor. In the bottom right figure, streptavidin was observed to bind to the selectively biotinylated surfaces, indicating the attachment of streptavidin is specific to the biotinylated surfaces.

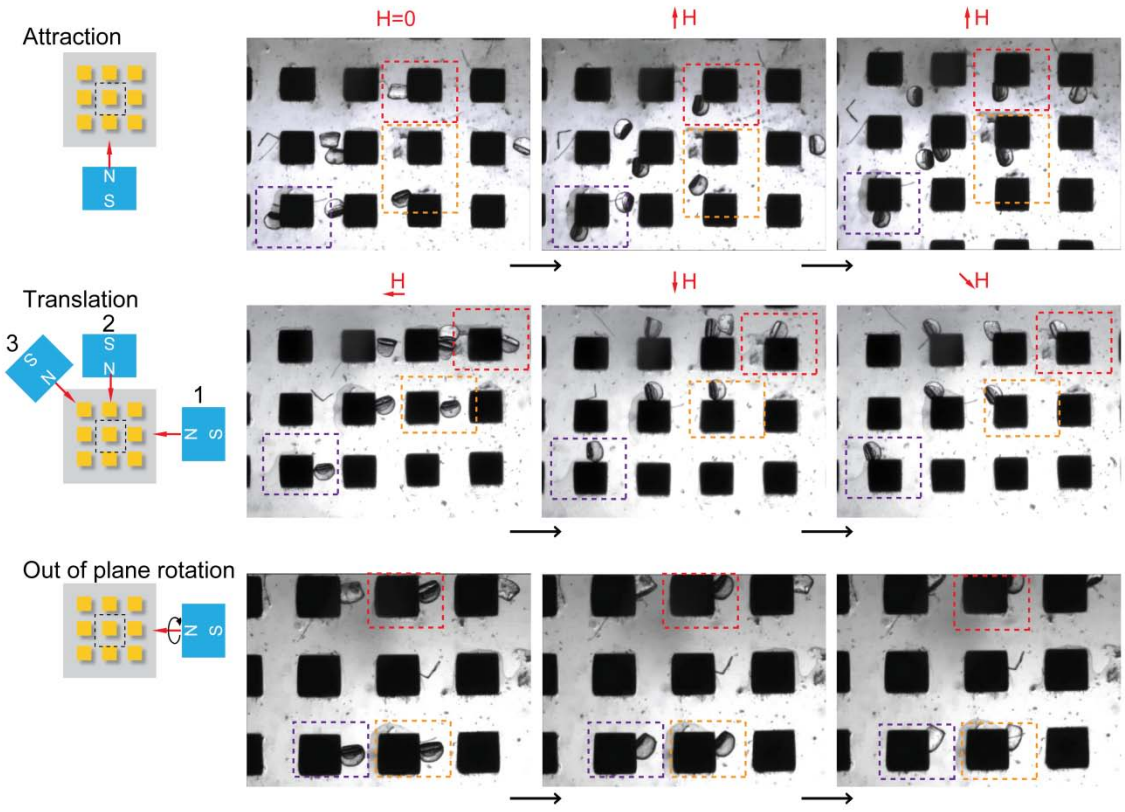

Figure S4. Manipulation of shaped magnetic microparticles over a micromagnet array. In the top row, the application of magnetic field attracted 5 particles, out of 7, at the corners of the magnetic elements with a 90 degree orientation. In the middle row, all 6 particles were moved along the edge of the magnetic elements following a change in magnetic field direction. In the bottom row, 3 particles in the field of view were flipped by rotating the magnetic field.

Bibliography

[1] R. Langer, D. A. Tirrell, Nature 2004, 428, 487; S. Mitragotri, J. Lahann, Nat Mater 2009, 8, 15.

[2] S. E. Chung, W. Park, S. Shin, S. A. Lee, S. Kwon, Nat Mater 2008, 7, 581.

[3] Y. Lu, Y. D. Yin, Y. N. Xia, Adv Mater 2001, 13, 415; J. F. Galisteo-Lopez, M. Ibisate, R. Sapienza, L. S. Froufe-Perez, A. Blanco, C. Lopez, Adv Mater 2011, 23, 30.

[4] D. C. Appleyard, S. C. Chapin, R. L. Srinivas, P. S. Doyle, Nat Protoc 2011, 6, 1761.

[5] J. Lee, P. W. Bisso, R. L. Srinivas, J. J. Kim, A. J. Swiston, P. S. Doyle, Nat Mater 2014, 13, 524.

[6] W. E. Uspal, H. B. Eral, P. S. Doyle, Nat Commun 2013, 4.

[7] Y. Geng, P. Dalhaimer, S. S. Cai, R. Tsai, M. Tewari, T. Minko, D. E. Discher, Nat Nanotechnol 2007, 2, 249; J. A. Champion, Y. K. Katare, S. Mitragotri, J Control Release 2007, 121, 3; S. C. Balmert, S. R. Little, Adv Mater 2012, 24, 3757; T. J. Merkel, S. W. Jones, K. P. Herlihy, F. R. Kersey, A. R. Shields, M. Napier, J. C. Luft, H. L. Wu, W. C. Zamboni, A. Z. Wang, J. E. Bear, J. M. DeSimone, P Natl Acad Sci USA 2011, 108, 586; G. Sharma, D. T. Valenta, Y. Altman, S. Harvey, H. Xie, S. Mitragotri, J. W. Smith, J Control Release 2010, 147, 408.

[8] I. A. Eydelnant, B. B. Li, A. R. Wheeler, Nat Commun 2014, 5; L. Leng, A. McAllister, B. Y. Zhang, M. Radisic, A. Gunther, Adv Mater 2012, 24, 3650.

[9] S. V. Murphy, A. Atala, Nat Biotechnol 2014, 32, 773.

[10] D. Dendukuri, D. C. Pregibon, J. Collins, T. A. Hatton, P. S. Doyle, Nat Mater 2006, 5, 365.

[11] K. W. Bong, K. T. Bong, D. C. Pregibon, P. S. Doyle, Angew Chem Int Edit 2010, 49, 87.

[12] K. W. Bong, D. C. Pregibon, P. S. Doyle, Lab Chip 2009, 9, 863.

[13] J. K. Nunes, C. Y. Wu, H. Amini, K. Owsley, D. Di Carlo, H. A. Stone, Adv Mater 2014, 26, 3712.

[14] A. L. Thangawng, P. B. Howell, J. J. Richards, J. S. Erickson, F. S. Ligler, Lab Chip 2009, 9, 3126; D. A. Boyd, A. R. Shields, P. B. Howell, F. S. Ligler, Lab Chip 2013, 13, 3105.

[15] K. S. Paulsen, D. Di Carlo and A. J. Chung, Nat Commun 2015.

[16] H. Amini, E. Sollier, M. Masaeli, Y. Xie, B. Ganapathysubramanian, H. A. Stone, D. Di Carlo, Nat Commun 2013, 4.

[17] A. D. Stroock, S. K. W. Dertinger, A. Ajdari, I. Mezic, H. A. Stone, G. M. Whitesides, Science 2002, 295, 647; P. B. Howell, D. R. Mott, S. Fertig, C. R. Kaplan, J. P. Golden, E. S. Oran, F. S. Ligler, Lab Chip 2005, 5, 524.

[18] D. Stoecklein, C. Y. Wu, K. Owsley, Y. Xie, D. Di Carlo, B. Ganapathysubramanian, Lab Chip 2014, 14, 4197.

[19] D. R. Mott, P. B. Howell, J. P. Golden, C. R. Kaplan, F. S. Ligler, E. S. Oran, Lab Chip 2006, 6, 540.

[20] P. Tseng, I. Pushkarsky, D. Di Carlo, Plos One 2014, 9.

[21] W. A. Braff, M. Z. Bazant, C. R. Buie, J Fluid Mech 2015, 767, 85.

[22] D. R. Griffin, W. M. Weaver, P. O. Scumpia, D. Di Carlo, T. Segura, Nat Mater 2015, 14, 737.

[23] H. O. Jacobs, A. R. Tao, A. Schwartz, D. H. Gracias, G. M. Whitesides, Science 2002, 296, 323.

[24] Y. D. Hu, J. Y. Wang, C. N. Li, Q. Wang, H. Wang, J. T. Zhu, Y. J. Yang, Langmuir 2013, 29, 15529.

[25] H. Lee, J. Kim, H. Kim, J. Kim, S. Kwon, Nat Mater 2010, 9, 745.

[26] N. Weber, D. Hertkorn, H. Zappe, A. Seifert, J Microelectromech S 2012, 21, 1098.

[27] J. C. Breger, C. Yoon, R. Xiao, H. R. Kwag, M. O. Wang, J. P. Fisher, T. D. Nguyen, D. H. Gracias, Acs Appl Mater Inter 2015, 7, 3398.

[28] D. Stoecklein, C.-Y. Wu, D. Kim, D. Di Carlo, and B. Ganapathysubramanian1, Under preparation 2015.

[29] C. H. Hsu, A. Folch, Appl Phys Lett 2006, 89.

[30] P. Tseng, J. Lin, K. Owsley, J. Kong, A. Kunze, C. Murray, D. Di Carlo, Adv Mater 2015, 27, 1083.

We have demonstrated the fabrication method and results of unique 3D shaped microparticle using optical Transient Liquid Molding in the previous paper. In the next paper, we focused on solving the adherent-cell-handling issue in the modern biomedical and clinic fields using 3D microcarriers, which can be fabricated only by the optical Transient Liquid Molding. The microcarrier was designed to not only allow cells growing and proliferate on a protected region but also be self-aligned in channel flow. We improved the fabrication system by increasing the throughput by two orders of magnitude for repeated biological experiments. We performed particle-based cell culture using large amount of 3D microcarriers, demonstrated the significance of the protective design, and executed high-speed imaging of adherent cells on the self-aligned microcarriers.

Chapter 4 :

3D Microcarriers for Adherent Cell Culture and Analysis

Abstract

Standard tissue culture and analysis of adherent cells is known to poorly replicate physiology and lead to cell damage, especially for primary or differentiated cell populations. We present an approach to scale up the manufacture of 3D-shaped hydrogel cell carriers. Particles are designed with a recessed nook in the first dimension to provide a tunable growth surface as well as shelter from fluid shear stress during processing by standard pipetting and flow cytometry. Particles are shaped in the orthogonal direction to allow for self-alignment in a confined flow, important for imaging flow cytometry. The desired asymmetric dumbbell shape was defined and the inverse problem was solved using a genetic algorithm to yield a sequence of pillars that closely recapitulated the desired shape. The precise 3D shapes of the cell carriers solve fundamental challenges with cell damage on the surface of previous planar cell carriers and is poised to enable the adoption of cell carriers for adherent culture, analysis, and sorting for large scale propagation and growth of a variety of adherent cells with less enzymatic passaging and improved physiological control.

Introduction

Traditional processes of tissue culture of adherent cells makes use of cell growth on flat and rigid polymer petri dishes, flasks and well plates. While cell analysis involves scanning the culture surface with microscopy or bringing cells into suspension with

enzymatic or physical treatments followed by flow cytometry to select sub-populations. This paradigm of cell culture, single-cell enzymatic suspension, and passaging is especially challenging for growth of terminally differentiated cell populations from pluripotent or multipotent precursors [1]. For example, the isolation of retinal pigmented epithelial cells derived from induced pluripotent stem cells cannot be accomplished using standard approaches but instead requires growth on surfaces followed by manual selection and scraping of pigmented clusters of cells for expansion.

Particle-based cell culture, whereby adherent cells grow and are analyzed on engineered microparticles or microcarriers, can serve as a new paradigm to accelerate culture, passaging, and analysis without exposing cells to harsh environments [2]. Spherical microcarriers, shown on the left hand side of Fig. 1(a), provide a high surface area enabling scaled-up production of anchorage-dependent cells [3]. Additional features can expand the capabilities of these microcarriers, for example, photonic crystal encoding enables evaluation of growth on multiple biomaterials simultaneously [4]. In the past decade, approaches to fabricate microparticles with non-spherical shapes has yielded more advanced functionalities for cell culture, manipulation and analysis, which allows refined exploration of cellular biology using engineering approaches. Sensitive stem cells can be cultured and investigated at the single cell level using magnetic micro-rafts [5]. Octopus-shaped microparticles provide a new cell-capture strategy for characterizing circulating tumor cells [6]. Interlocking 2D extruded microparticles with cells embedded allow self-assembly to generate a spatial distribution of various cell types, which is promising for applications in tissue engineering [7].

However, the current capabilities of microparticles have been limited by the ability to engineer the shape and functionality of microparticles in all three dimensions.

To achieve adherent cellular analysis in a precise and high throughput manner, there is need to develop engineered microcarriers that can enable growth but also integrate with the advantages of high content screening and flow cytometry: gathering comprehensive information and detecting signals at high speed simultaneously. The carrier should possess three integrated capabilities: (i) allow cell adhesion and growth, (ii) protect cells from shear stress intrinsic to pipetting and flow through single-point and imaging flow instruments, and (iii) enable alignment in a microchannel flow cell to achieve uniform velocities necessary for imaging cytometry readout [8]. Cell culture should be possible in a protected area while the shape of the carrier self-guides it toward a constant lateral location in channel flows, such that adherent cells can pass through a fixed imaging field of view at a uniform velocity for continuous detection. Through this process, cultured cells should be protected from interaction with flow cell walls or high shear-stress from flow fields around the carrier.

We design a 3D shaped microparticle, which acts as a microcarrier for cell culture and analysis. The microcarrier is designed to have a localized area of extracellular matrix for cell adhesion and culture in a shear-protected nook, which allows high-speed transportation and imaging of adherent cells in channel flows with minimized shear stress. The microcarrier is shaped by the orthogonal intersection of two 2D patterns.

One pattern allows for the alignment of the microcarrier in flow and provides an isolated cell culture region while the other has a depressed region to serve as a shear stress shelter with a width designed to match the dimensions of a microchannel and allow for ‘quasi-two-dimensional’ motion in flow (Fig. 1(a)). To align in flow we design the pattern in one dimension with an asymmetric dumbbell shape which has been shown to self-align in Stokes flows [9]. A cell adhesive region is designed to be encapsulated inside the boundary of this shape and surrounded by a region of polymer with low binding affinity. In the orthogonal direction, the shear-sheltering region consists of notches on both sides of a rectangular shapewith a height designed to be 90% of the height of the microchannel flow cell. The lateral position and length of the notches are aligned with the cell adhesive region patterned in orthogonal projection.

Microcarrier Fabrication.

We make use of a novel microparticle manufacturing approach, called optical Transient Liquid Molding (OTLM), that enables producing new classes of complex microparticles with software-designed 3D shape and functionality [10]. OTLM generates microparticles by illuminating patterned UV light onto a target flow stream of polymer precursor with a pre-engineered cross-sectional pattern shaped in a microchannel. Inertial flow deformation around micropillars is used to sculpt the cross-sectional pattern of co-flows (streams of photo-crosslinkable monomer with and without photoinitiator) as a single phase at Reynolds (Re) number between 1 to 100 [11]. Because of the irreversibility of the flow, we break aft-fore symmetry, generating net secondary flows in the cross-

sectional plane which depend on the location and size of the micropillars. By eliminating the hydrodynamic coupling between micropillars, we can engineer and predict the cross-sectional pattern of the target flow in a rapid manner using software, uFlow, developed in our lab, which we have made open to use by the public: http://biomicrofluidics.com/software.php. We have demonstrated that fundamental and complex patterns can be created by arranging the size and sequence of micropillars [11, 12]. To produce complex microparticles, we developed an automated fluidic and optical system, OTLM, where upstream/downstream pressure and optical shutters are controlled using LabVIEW. Once the designed cross-sectional pattern is developed completely in the flow, we impede the flow by equalizing the upstream and downstream pressure and then apply UV illumination through a mask to photocrosslink microparticles in the microchannel. OTLM generates microparticles with levels of asymmetry previously unachievable using flow lithography techniques, with shapes formed by the intersection of two extruded 2D patterns. The approach also allows hybrid particles with multiple functionalities based on differences in content of the co-flowing streams, including biotinylated surfaces and shape-dependent magnetic properties on an individual microparticle [10, 13].

Genetic algorithm to solve the inverse problem.

We design an asymmetric dumbbell shape by using a genetic algorithm to solve the inverse problem and identify positions of pillars within the microchannel that satisfy the constraints of our desired shape without user-based iterations. Previous work using

OTLM and uFlow required the user to experiment with a variety of micropillar configurations in order to arrive at a desired cross-sectional shape, a process which could be tedious or difficult to achieve given the extremely large design space ($(4x8)^{10}=1.13x10^{15}$ possible configurations for an 10-pillar sequence). We had a choice to design either of the two orthogonal shapes, asymmetric dumbbell or notched rectangle, with inertial flow deformation. Given our previous experience that smooth curved shapes require fewer pillars to achieve, we chose to design the asymmetric dumbbell in the flow direction. To achieve the design without manual iteration, we applied a genetic algorithm approach to reach an optimized initial condition and micropillar sequence. The genetic algorithm defined a set of volumetric flow rate ratios for streams with and without photoinitiator at the inlet (called the inlet pattern) and the pillar sequence to achieve the desired outlet pattern based on a cost function. After the program executing the genetic algorithm generated several sets of solutions, we fed the solutions respectively into uFlow, and designed the volumetric flow rate of a sub-stream that included biotin which we used for the cell adhesive region in the final particle. Finally, we designed the optical mask for the orthogonal projection of the microcarrier that included a notched rectangle to achieve the shear-stress-shelter pattern . Here we set the length of the rectangle to be the same with the asymmetric dumbbell with the notches located at the same lateral position of the cell adhesive region. The figure on the right hand side of Fig. 1(b) demonstrates the 3D shape of the microcarrier for the final design predicted by uFlow.

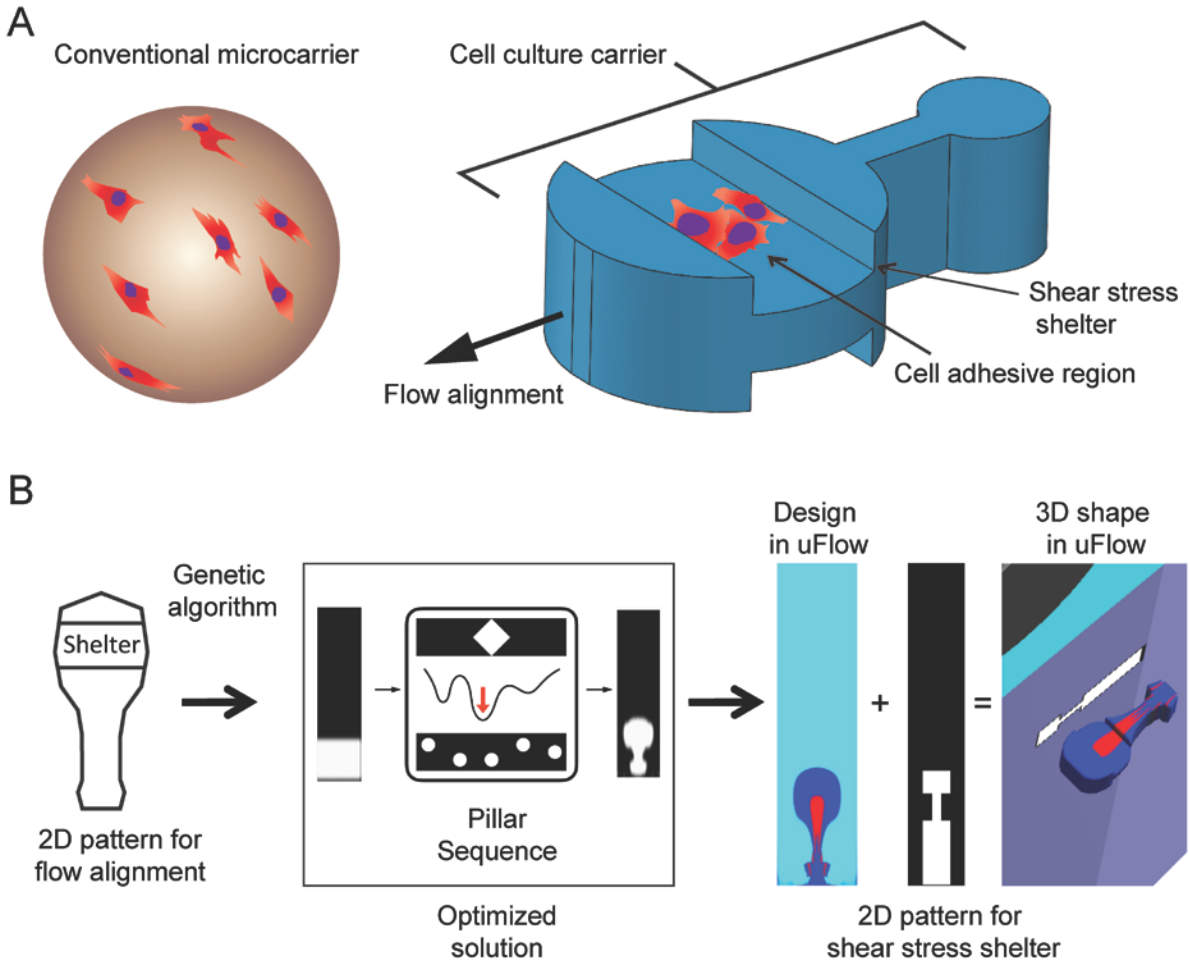

Figure 1: Design of 3D microcarriers. (a) Conventional spherical microcarrier (left hand side) and a novel microcarrier (right hand side) with integrated functionalities achieved by 3D shaping: cell culture, shear stress shelter, and flow alignment. (b) Design flow chart based on the characterization of optical Transient Liquid Molding. To generate dumbbell shape using inertial flow engineering, a genetic algorithm is executed to optimize the design parameters, including the inlet pattern and pillar sequence. uFlow is used to demonstrate the final dumbbell shape with cell adhesive region (red) and 3D shape of the microcarrier by applying the shelter design.

Expanding fabrication throughput for cell culture

To generate 3D shaped microcarriers at a larger scale needed for repeated biological experiments, we developed a new version of OTLM which achieved a two order of magnitude increase in production rate compared to previous demonstrations (Fig. 2(a)). In the fabrication system, Poly (ethylene glycol) diacrylate (PEGDA, Mn~575) and 2,2-Dimethoxy-2-phenylacetophenone were used for the monomer and photoinitiator in the co-flow respectively. Biotin-PEG-Acrylate was synthesized as an additive to form the cell adhesive region in the target particle. We took advantage of the high Peclet number of our flow which allowed for the fully-developed sculpted flow to maintain its shape for a long channel length downstream. This allowed us to significantly enhance the fabrication rate by synthesizing one hundred microcarriers per exposure, instead of one, in an elongated straight microchannel downstream of the flow sculpting region. The novel fabrication system required a longer microfluidic chip which we fabricated using 6-inch wafer-based soft lithography as well as a collimated UV light source with a large exposure area to expose the sample through an optical mask with hundreds of patterns in a linear array.

We first investigated the dimensional error in fabrication caused by diffusion of photoinitiator laterally into the monomer stream without photoinitiator along the microchannel, potentially expanding the shape in downstream regions of the flow where diffusion time is longer. Finite element method simulations of the coupled fluid flow and convection-diffusion problem identified that for our operating conditions ($Pe=2.88x10^6$,

Pe=UW/D) the central interface along a cross section of the co-flow shifts ~10 μm 4 cm downstream, for an average downstream velocity, U of 0.24 m/s, channel width, W of 1200 μm, and diffusivity of the photoinitiator, D of ~ 10^{-6} cm^2 s^{-1}. When lengthening the channel further from 4 cm to 24 cm downstream only an additional 5 μm expansion in the photoinitiator stream width of was observed. Considering microcarriers with dimensions of 200 μm, the dimensional error at these two locations are 5% and 7.5% respectively, indicating the dimensional variation of microcarriers fabricated along the sculpted flow for significant distances downstream would be negligible. Supported by the simulation results, we enlarged the length of the region downstream of the sculpted flow to include a straight channel with a length of an additional ~4 cm downstream, which also required modifications to the optical exposure system. Given the simulation results for 24 cm channel lengths, we expect further increases in throughput, up to another order of magnitude would be possible by further extending the length of the channel.

Using the new high-throughput process we determined that particle dimensions and patterns were largely uniform. Following 30 minutes of fabrication we were able to produce ~18,000 number of particles, such a large amount of microcarriers that it was visible at the macro scale in a conical tube. Images of the particles qualitatively indicate that the orthogonal flow-alignment and shear-stress-shelter patterns match the predicted design for each microcarrier. The uniformity of the flow-alignment pattern of each microcarrier, which is most dependent on diffusion of photoinitiator downstream, was quantitatively studied using image traces of the boundaries. The averaged

deviation of the distance between the boundaries and mass centers is ~12μm, which is negligible comparing to the dimension of the dumbbell shape. Lastly, we verified that the biotinylation of the cell adhesive region was uniform by incubating the microcarriers with fluorescently-labeled streptavidin. The red pattern on every microcarrier occupied the same region of the particle (averaged correlation of each pattern and averaged pattern>0.8) in agreement with our design in Fig. 1(b).

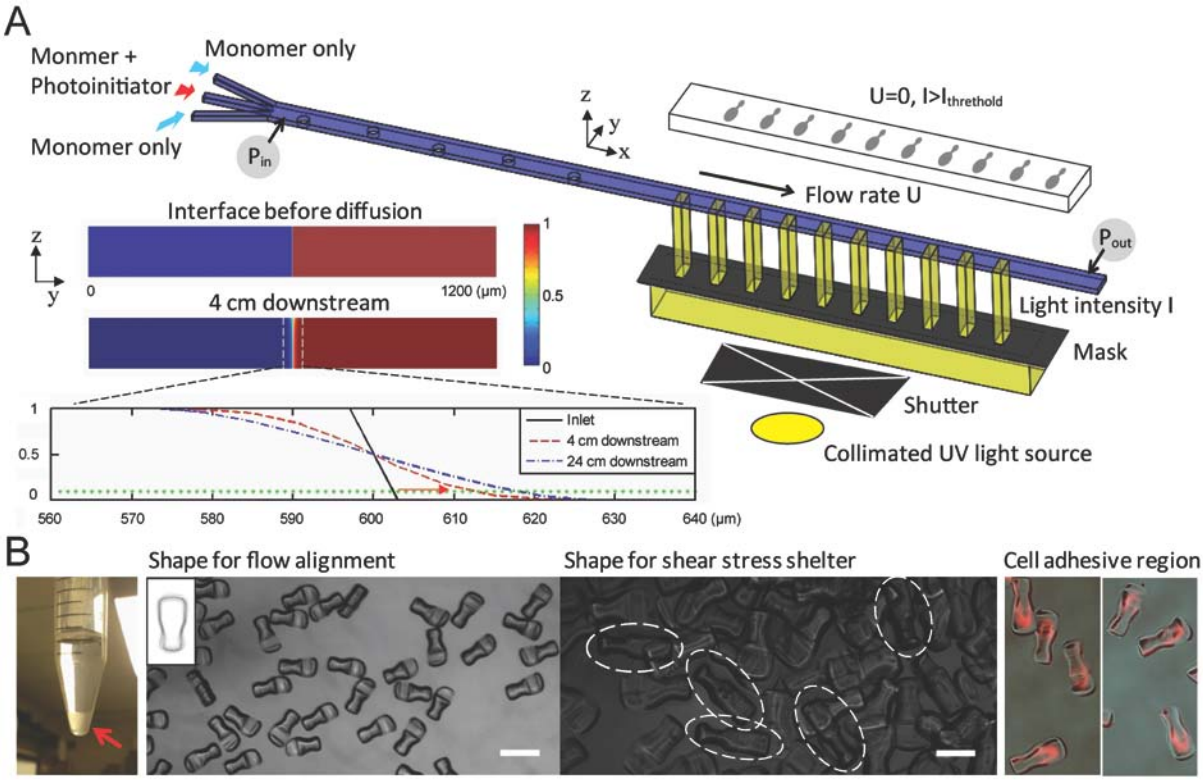

Figure 2: Schematics, simulation, and results of new version of OTLM. (a) Fabrication system includes a microfluidic channel with long length downstream, flow handling (pumping and stopping by altering P_{in} and P_{out}), and UV illumination through a linear array. In the inset on the left hand side, a convection-diffusion simulation result shows that the diffusion length in the lateral direction of a middle interface in the microchannel at high Pe is less than 10% dimension of fabricated microcarriers, so the dimensional error in a linear array (each flow stopping) is negligible in theory. (b) Images of

fabricated microcarriers at macro and micro scale. Accumulated microcarriers in a tube, microcarriers with flow alignment (400 µm scale bar) and shelter (200 µm scale bar) design imaged using microscopy, and fluorescent-labeled cell adhesive region are shown from left to right hand side.

Self-alignment of microcarriers in channel flows

An important aspect of the microcarrier design, is to allow alignment in a microchannel flow cell for imaging cytometry applications that rely on uniform velocity and a defined imaging field of view. We evaluated the performance of the asymmetric dumbbell flow-alignment design with fabricated microcarriers. We pumped microcarrier-laden solution into a long straight flow-through microchannel and observed focusing and alignment using a high speed camera under various flow conditions. The microchannel had dimensions of 600 µm width by 150 µm height to match the height of the fabricated microarriers. In Fig. 3(b), a time-lapse image shows that at low flow rates microcarriers will rotate until reaching a horizontal configuration self-aligned with the flow, with the larger lobe of the dumbbell facing downstream. For higher flow rates useful for higher-throughput cytometry (channel Re ~20) we observed rotational and positional alignment within the channel at the inlet and 4 cm downstream. . The traced boundaries of the particles at the inlet spanned across the whole channel width while 4 cm downstream the traces converged into the flow-alignment pattern at the center of the channel with the large lobe facing downstream. These results support that the designed pattern enables self-alignment by hydrodynamically interacting with the channel flow. The lateral locations of the centers of mass and orientations of the imaged microcarriers also

confirm these results quantitatively (Fig. 3(c) and (d)). Compared with wide distributions at the inlet (green), the distributions became significantly tighter downstream (blue) around the centerlocation of the channel and zero degree alignment with the large lobe facing downstream. Imaging flow cytometry systems, i.e. FIRE and Amnis ImageStream [14] benefits from a relatively uniform velocity of flowing targets, which can be enabled particle alignment. We calculated the velocity of microcarriers and as can be seen in Fig. 3(e), the velocity distribution was also relatively narrow and there was a peak velocity of ~65 mm/s, promising for future integration. In addition, for generally understanding the flow behavior of the asymmetric dumbbell shape, we investigated the alignment quality as a function of the flow speed of the microcarriers. The relatively uniform behavior across flow velocities (~20 mm/s -~1000 mm/s) indicates that the fish-shaped microcarriers can be robustly self-aligned even if there are velocity fluctuations in the system.

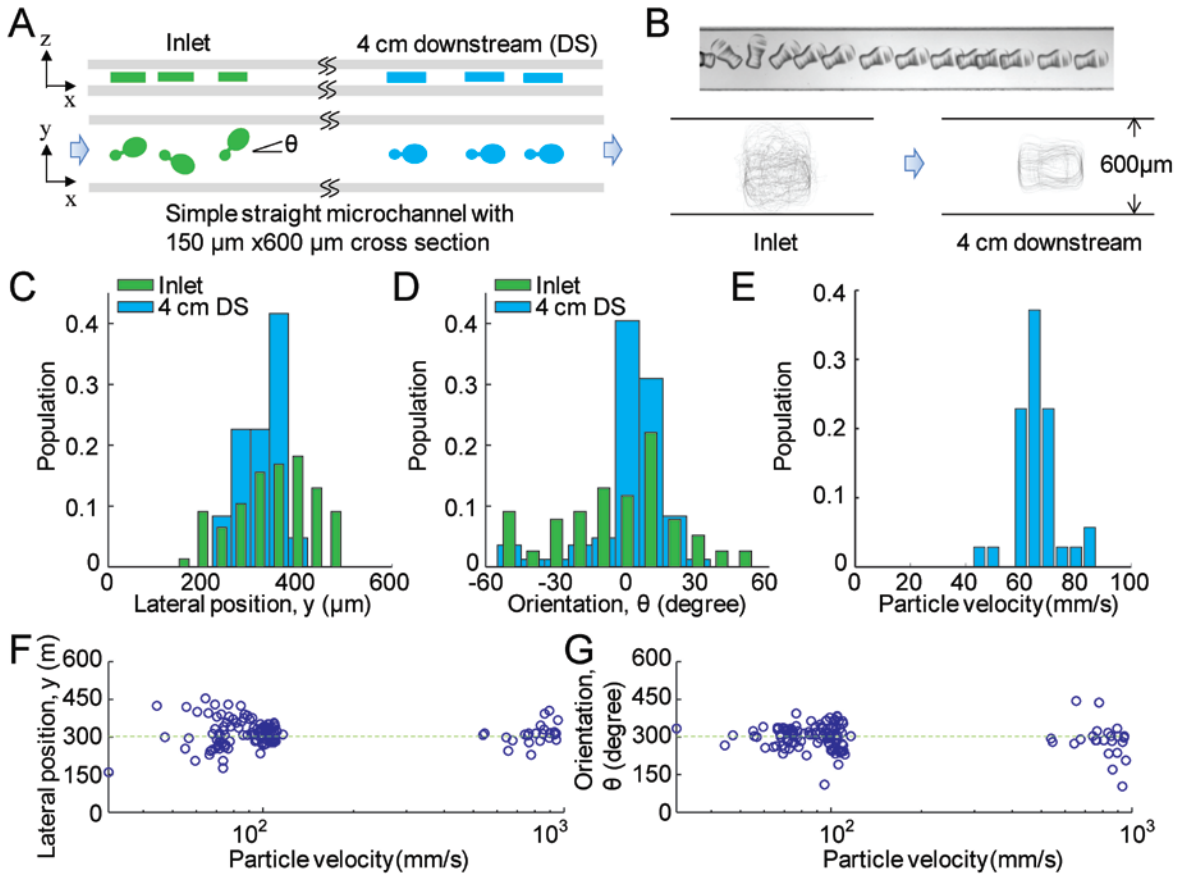

Figure 3: Flow behaviors of microcarriers in various conditions of channel flow. (a) Schematic of top and side views of the microcarriers flowing from inlet to 4 cm downstream in a straight microcahnnel. (b) Time-lapsed image (top inset) of a microcarrier self-aligning at low Re in the channel with 600 μm wide at the position close to the inlet and overlapped boundaries (bottom insets) of microcarriers flowing at the inlet and 4cm downstream at Re~20. (c, d, e) Lateral positions, orientations, and velocity of microcarriers in the bottom case of Fig. 3(b), quantitatively showing the behavior of self-alignment and uniform velocity distribution at Re~20. (f, g) Lateral positions and orientations of numerous microcarriers flowing at different velocities in a manually-pumping experiment, quantitatively showing the behavior of self-alignment at wide ranges of Re.

Shear-protected growth of cells on microcarriers

To study cell culture on microcarriers and evaluate whether there was a differential survival advantage for cells adhered in the nook area of the microcarrier we created particles with biotin/collagen coating over the entire particle. Following incubation of cells with collagen patterned microcarriers we observed cell attachment and growth over several days (Fig. 4(a)(i)). Cells remained viable during this time period and proliferated (Fig. 4(a)(ii)). After incubation of several days, the cells can reach confluency over the entire microcarrier (Fig. 4(a)(iii)). We observed that standard processes of pipetting and liquid-handling, dislodged cells from most regions of the microcarriers, however, we observed that cells were differentially enriched in the area with low shear stress, which includes the shelter and side surface (Fig. 4(a)(iv)). These cells also remained viable. While the design of shear stress shelter functioned as expected, the waist of the dumbbell shape also was observed to provide a sheltering effect and lead to enhanced cell adhesion.

We next demonstrated adherent-cell brightfield imaging flow cytometry by pumping medium with microcarriers through a microfluidic flow cell. In these experiments the patterned adhesive region was included to encourage growth only in the protected shelter of the carrier. The images in Fig. 4(b) show that MDA-MB231 cells can be imaged in a high-speed flow with clear morphology. Adherent cells were rapidly transported in the straight microchannel and occupied the same focal plane and within a narrow imaging window of ~300 μm using 3D shaped microcarriers. To investigate cell

viability, we collected cell-loaded microcarriers after flowing through the microchannel and continued culture for 2 days. Cells adhered in the shelter remained viable by live-dead stain and continued to proliferate (Fig. 4(c)). This data suggests that physical interaction with flow channel walls and fluid shear stress induced by flow was lower than the critical threshold causing cell death for cells adhered in the shear sheltering region.

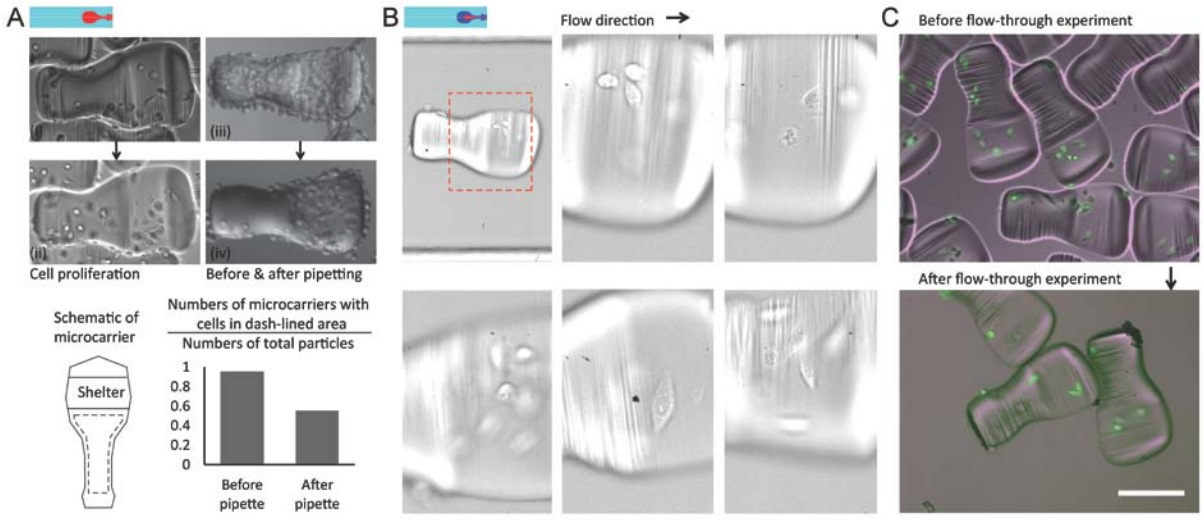

Figure 4: Cell adhesion, proliferation, protection, and analysis using 3D microcarriers. (a) Cell attachment and growth in the shelter after incubation with microcarriers and suspended cells (i-ii), and cell protection provided by the shear stress shelter during pippetting and liquid-handling (iii-iv). (b) High speed imaging of the adherent cells on the microcarriers flowing through the straight microchannel. (c) Viable adherent cells in the shear stress shelter after the flow-through experiment. The scale bar is 200 µm.

Discussion and Conclusion

We demonstrated a novel type of 3D microcarrier allowing mobile particle-based cell culture, rapid transportation and high speed analysis of adherent cells with minimal forces acting on cells. We adapted an unique microparticle fabrication technology, high throughput optical Transient Liquid Molding, to manufacture microcarriers in a rapid manner with high fabrication quality. Adherent cells were shown to grow, proliferate, protected, manipulated, and analyzed inside the designed shear stress shelter of the microcarrier. In the short term, it is promising to integrate the microcarrier system with advanced optic equipment, for example, FIRE and Amnis ImageStream, for particle-based high content screening, which can be applied to accelerate the drug discovery in the pharmaceutical industry. In the long term, we are proposing to utilize the integrated system to analyze and isolate specific population differentiated from stem cell precursors for benefiting regeneration medicine.

Acknowledgement

The authors thank Harsha Kittur for discussing and assisting on cell culture, Jonathan Lin for assisting coding in Matlab, Manjima Dhar for suggestion of tubing selection, Janay Kong and Dr. Westbrook Weaver for suggestions of chemical preparation, and Mr. Elias Sideris at UCLA for the viscosity measurements. This work is partially supported by a grant from the National Science Foundation (NSF 1307550).

Methods

High-throughput optical Transient Liquid Molding and microcarrier fabrication

High-throughput optical transient liquid molding includes microfluidic chip with pillar design, flow pumping/stopping setup, and collimated UV light setup. The microfluidic chip was placed on a xy-translational and rotational optical stage as the polymeric precursor liquid (PEGDA with and without photoinitiator) were injected from the bottom of the chip. Particles and unpolymerized waste solution was also exhausted out of the bottom of the chip passed a pinch valve toward a collection tube. In addition, to match the need for increased optical exposure area, we generated collimated UV light in a circle with a 3 cm diameter on the top of the chip with a high power UV light source and collimation adaptor (Excelitas Technologies, OmniCure ® S2000 UV Curing System and Adjustable Spot Collimating Adaptor). Instead of projecting one UV light pattern onto the sculpted flow using a mask in the conjugate image plane of the sample in the previous version of fabrication, we illuminated collimated UV light through a chrome optical mask, which was placed on the top of the glass substrate of the chip with hard contact. Parallel mask patterns in a linear array were aligned with the channel sculpted flow. We designed alignment marks on the mask and microfluidic chip so the masked patterns could be registered to the same lateral position of the sculpted flow from the first to the last pattern. To verify the collimation, we synthesized 2D extruded microparticles using stationary monomer with photoinitiator inside a microchannel. The tilting angle of the vertical walls of the microparticles was observed to be within ~10 degrees, confirming the collimation. The fluidic and optical setup were controlled with a LabVIEW code to automate the fabrication process with the following sequential steps: (i) pumping the co-

flow using a syringe pump, (ii) stopping flows by stopping pumps and pinching tubing with a pinch valve downstream, (iii) illuminating the flow by opening a shutter mounted below the collimation adaptor, (iv) pumping the solutions again to wash out the cured microcarriers into a conical tube and to rebuild the sculpted flows, and then repeating these steps (i-iv) for multiple cycles. After the final cycle of the process (typically 100 cycles, yielding 10,000 number of microcarriers), the tube was centrifuged at 2500 rpm for 5 minutes to pull microcarriers down to the bottom of tube. We then removed supernatant and executed a rinse process with three repeats to remove residual precursor using DPBS with 0.1% pluronic. The rinse process included resuspending microcarriers in bulk solution, centrifuging microcarriers down to sediment, and pipetting out the supernatant gently to avoid withdrawing microcarriers.

Comsol simulation of convective diffusion

To simulate the fabrication error caused by convective diffusion of photoinitiator, we utilized a finite element method model solving the full 3D incompressible Navior-Stokes equations coupled with 3D diffusion equations in COMSOL Multiphysics. We run a simulation of flow model, fully developed at inlet and outlet, in a rectangular microchannel with 1200μm wide, 300μm height, 2000μm long, and then one of convective diffusion model based on the flow field in the microchannel by setting the concentration of photoinitiator on the left and right hand side to be 0 and 1. We programmed a script to iterate mapping the outlet concentation to the inlet one and run the simulation of convective diffusion repeatedly based on the same flow field in the

microchannel until reaching the channel length fabricated in reality. We extracted out the concentration distribution for different number of iterations to evaluate the degree of fabrication error in different channel length.

Analysis of the fabrication quality

We took images of microcarriers and fluorescent cell adhesive region and programmed Matlab codes to determine the fabrication quality. We diluted the microcarriers, spread a droplet of solution with microcarriers on a microscopy slide, and sandwiched the solution with a cover slide to align carriers for imaging, and then repeated these steps to obtain multiple images while minimizing the overlap between microcarriers in each microscopic image. With several images of microparticles using a 4X objective, we used a Matlab code to detect the boundary of each microcarrier and for each enclosed boundary rotate it until the aspect ratio reaches a maximum value to allow all boundaries to be aligned in the vertical orientation. We overlapped all the detected boundaries using the same mass center and calculated an averaged deviation of the boundaries to qualitatively and quantitatively describe the fabrication quality. The averaged deviation of the boundaries is defined as the average, over 360 degree, of the deviation of the distance between the single point on the boundary and the mass center at an angle of all detected boundaries. Moreover, we took bright-field and florescent images on the microcarriers, which was incubated with fluorescent streptavidin. We rotated and overlapped the fluorescent images with respect to the angle and mass center we processed for the bright-field images of microcarriers. To represent the

fabrication quality of the cell adhesive region, we calculated the average, over all microcarriers, of the 2D correlation between each image and averaged image.

Imaging and analyzing microcarriers flowing through a straight microchannel

We utilized a microscopy with high speed camera to record the images of the microcarriers flowing through a straight microchannel at inlet and 4 cm downstream. We pumped microcarrier-laden water manually and continuously using a syringe pump respectively for the case with various Re and contant Re (Re~20). A matlab code was programmed to extract the boundary of each captured microcarrier, calculate its lateral location, orientation, and velocity. The lateral location was determined by the mass center of the boundary while the orientation was gotten by searching the angle rotating related to the mass center to reach minimal aspect ratio. For particle velocity, we calculated the distance of a microcarrer between two sequential frames and multiplied it with the frame rate of the video.

Cell adhesion with microcarriers

To demonstrate the cell binding with microcarriers, cell culture on microcarriers, and high speed imaging of cells on flowing microcarriers, we chose MDA-MB-231 breast cancer cells for cell adhesive experiments. We sequentially incubated microcarriers with 1mg/mL streptavidin and then biotinylated collagen I for overnight. The biotin-collagen was synthesized by mixing solutions of biotin-NHS and collagen for overnight, and the

non-reacted biotion-NHS was got rid of using standard dialysis process. After each incubation, we rinsed carriers using DPBS solution (0.1% pluronic) with volume 100 times larger than the volume of solution with microcarriers. We then used DMEM solution (0.1% pluronic) to rinse microcarriers, transferring them into medium solution. Microcarriers were first settled down on the bottom of an ultra low attachment well (Corning Inc., Corning ultra low attachment surface culture dish, 96-well plate), and then 100 µL medium solution of suspending cells with concentration of $4x10^4$/mL was dispensed. After overnight incubation, we took images on microcarriers, showing that cell resided and spread out on the surface of microcarriers.

Cell protection by the design of the shear stress shelter

To investigate the shear-stress-protection effect caused by the shelters, we first analyzed the cell occupancy on the area of the microcarrier without protection. We produced microcarriers with collagen on all surfaces, seeded and incubated with cells to encourage growth randomly on the surfaces. We then pipetted the microcarrier-laden medium up and down using 100µL pipette tip, suspended microcarriers in the bulk medium, settled them back to the well, and imaged the cells on microcarriers. We counted the microcarriers with cells outside the shear shelters before and after pipetting/washing and divided it over the total number of microcarriers. To simplify the discussion, we excluded the surface area close to the side surface and only searched for cells residing on the top and bottom flat surfaces of the microcarrier, as the area enclosed by dash lines in Fig. 4(a).

Imaging microcarriers with cell adhesion flowing through a straight channel

We pumped the medium with cell loaded microcarriers into a straight microchannel to image the adhesive cells on the self-aligned microcarriers. In order to prevent expansion of hydrogel particles caused by temperature change during incubation and enable better matching of dimensions and flow-alignment, we equilibrated cell loaded microcarriers at room temperature for 15 minutes. We then suspended the microcarriers with cells in 500 µL medium, withdrew the solution into tubing with a 1.6 mm inner diameter and 1 m length (to prevent particle settling and loss in the syringe), plugged the tubing into the inlet of the straight imaging microchannel, and pumped the solution with a volume flow rate of 500 µL/min (Channel Re~20). We recorded videos 4 cm downstream in the microchannel using a high-speed camera and mercury light source with a short exposure time.

Bibliography

1. Lowry, W.E.; Richter, L.; Yachechko, R.; Pyle, A.D.; Tchieu, J.; Sridharan, R.; Clark, A.T.; Plath, K., “Generation of human induced pluripotent stem cells from dermal fibroblasts,” *Proc. Natl. Acad. Sci. U. S. A.*, 105, 2883–2888, 2008.
2. Christina L. Randall, Yevgeniy V. Kalinin, Mustapha Jamal, Tanmay Manohar, and David H. Gracias, “Three-dimensional microwell arrays for cell culture,” *Lab Chip*, 11, 127-131, 2011.
3. van Hemert P, Kilburn DG, van Wezel AL., “Homogeneous cultivation of animal cells for the production of virus and virus products,” *Biotechnol Bioeng.*, 11, 5, 875-885, 1969.
4. Liu W, Shang L, Zheng F, Lu J, Qian J, Zhao Y, Gu Z., “Photonic crystal encoded microcarriers for biomaterial evaluation,” *Small*, 10, 1, 88-93.
5. Gracz AD, et al, “A high throughput platform for stem cell-niche co-cultures and downstream gene expression analysis,” *Nat Cell Biol*., 17, 3, 340-349, 2015.
6. Chen L, et al, “Flexible Octopus-Shaped Hydrogel Particles for Specific Cell Capture,” *Small*, 12, 15, 2001-2008, 2016.
7. Yanan Du, Edward Lo, Shamsher Ali, and Ali Khademhosse, “Directed assembly of cell-laden microgels for fabrication of 3D tissue constructs,” *PNAS*, 105, 28, 9522-9527, 2008.
8. Eric D. Diebold, Brandon W. Buckley, Daniel R. Gossett, and Bahram Jalali, “Digitally synthesized beat frequency multiplexing for sub-millisecond fluorescence microscopy,” *Nature Photonics*, 7, 806-810, 2013.
9. Uspal, William E.; Eral, H. Burak; Doyle, Patrick S., “Engineering particle

trajectories in microfluidic flows using particle shape," *Nat. Commun*., 4, 2666, 2013.

10. Wu, Chueh-Yu; Owsley, Keegan; Di Carlo, Dino, "Rapid Software-Based Design and Optical Transient Liquid Molding of Microparticles," *Adv. Mater*., 27, 48, 7970-7978, 2015.
11. Amini H, Sollier E, Masaeli M, Xie Y, Ganapathysubramanian B, Stone HA, et al., "Engineering fluid flow using sequenced microstructures." *Nat. Commun*., 4, 2013.
12. D. Stoecklein, C.-Y. Wu, K. Owsley, Y. Xie, D. Di Carlo, and B. Ganapathysubramanian, "Micropillar sequence designs for fundamental inertial flow transformations," *Lab Chip*, 14, 21, 4197–4204, 2014.
13. Ki Wan Bong, Ki Tae Bong, Daniel C. Pregibon, and Patrick S. Doyle, "Hydrodynamic focusing lithography," *Angew. Chem. Int. Ed.*, 49, 87-90, 2010.
14. Maria E. Moreno-Fernandez, Jara J. Joedicke, and Claire A. Chougnet, "Regulatory T cells diminish HIV infection in dendritic cells – conventional CD4+ T cell clusters," *Frontiers in Immunology*, 5, 199, 2014.